quaternary

MDPI

Article

Holocene Aeolian Variability in Central Asia Inferred from Grain-Size End-Member Modeling of Sayram Lake Sediments

Shuang Yang, Yuchen Xu, Longjuan Cheng, Dongliang Ning, Dejun Wan and Qingfeng Jiang *

School of Geographical Science, Nantong University, 9 Seyuan Rd, Nantong 226019, China; 2435320118@stmail.ntu.edu.cn (S.Y.); 2235320133@stmail.ntu.edu.cn (Y.X.); longjuan822@ntu.edu.cn (L.C.); ningdl@ntu.edu.cn (D.N.); dejunwan@ntu.edu.cn (D.W.)

* Correspondence: qfjiangz@ntu.edu.cn

Abstract

Arid Central Asia (ACA) is a major source of atmospheric dust in the Northern Hemisphere; however, the evolutionary models and driving mechanisms of Holocene aeolian activity in this region remain debated. Based on 13 reliable AMS ^{14}C dates from the Sayram Lake SLM2009 sediment core, this study reconstructs the Holocene sequence in aeolian activity through end-member modeling analysis (EMMA). It evaluates its relationship with regional atmospheric circulation. Four end-members were identified from base to top: EM1, with a modal grain size of 7.58 μm, represents low-energy suspension deposition; EM2 (26.30 μm) reflects lacustrine hydrodynamic processes; while EM3 (52.48 μm) and EM4 (416.86 μm) serve as proxies for regional aeolian activity. The results indicate that aeolian activity was relatively strong during the early Holocene (reaching peaks at 11.7–11.2 and 9.2–8.1 cal ka BP), significantly intensified during the mid-Holocene (7.3–5.3 cal ka BP), and gradually weakened in the late Holocene (since 4.0 cal ka BP). Comparison of the aeolian record from Lake Sayram with Greenland ice cores, North Atlantic ice-rafted debris events, and the GISP2 K^+ record indicates that variations in aeolian activity in arid Central Asia are closely linked to the Northern Hemisphere climate system. We propose that these variations were primarily modulated by large-scale atmospheric circulation, driven by the synergistic interaction between the Siberian High and the mid-latitude westerlies.

Keywords: aeolian activity; Sayram Lake; end-member analysis; Holocene

1. Introduction

Atmospheric mineral dust serves a critical role in climate feedback systems via its impacts on radiative forcing, nutrient supply, and cryospheric albedo [1,2]. Arid Central Asia (ACA) represents a major global source of atmospheric mineral dust, and dust emitted from this region can be transported by atmospheric circulation to East Asia, the North Pacific, and even Greenland [3,4], thereby exerting significant influences on global biogeochemical cycles and climate variability [5,6]. Aeolian activity in arid regions is widely regarded as an important response indicator of global change and exerts a profound impact on ecological environments and the development of human societies. Its evolutionary history records the variations in regional climate systems. Therefore, investigating aeolian activity in arid Central Asia is important for understanding regional environmental change.

Over the past decades, numerous studies have investigated Holocene aeolian activity in the ACA using various geological archives. These reconstructions are primarily based on aeolian sedimentary records, including desert deposits, loess–paleosol sequences, and

Check for updates

Academic Editor: Pedro Proença Cunha

Received: 26 January 2026
Revised: 3 April 2026
Accepted: 7 April 2026
Published: 8 April 2026

lake sediments [7–13]. However, the evolution of Holocene aeolian activity in the region remains controversial. Evidence from loess sections in the Ili Basin [14], aeolian loess/sand sections near the Tukai Desert [15], sedimentary records from Shuanghu Lake in the Junggar Basin [16], and other regional archives [17–21] suggests relatively weak aeolian activity during the early to middle Holocene, followed by a marked intensification in the late Holocene. In contrast, records from Lake Ailike in the Junggar Basin [22] and a loess profile in the Ili Basin [23] indicate stronger aeolian activity in the early–mid Holocene, followed by a weakening in the late Holocene. A third pattern, inferred from the ShaYan loess section in southern Kazakhstan [24], suggests strong aeolian activity in the early Holocene, weakened activity during the middle Holocene, and renewed intensification in the late Holocene. These contrasting interpretations likely arise from the complexity of grain size proxies, which often integrate signals from multiple sedimentary processes and may introduce uncertainties when reconstructing aeolian dynamics.

Closed-basin lakes in arid regions provide valuable archives of past hydroclimatic and sediment-transport processes because lake sediments integrate signals from atmospheric circulation and catchment dynamics [25–27]. Owing to their relatively continuous sedimentation and high temporal resolution, lake sediments can preserve valuable records of past aeolian activity [28–30]. In this study, grain size end-member modeling analysis (EMMA) is applied to sediment core SLM2009 from Sayram Lake to isolate independent aeolian components from mixed sedimentary assemblages, providing a framework for evaluating Holocene aeolian variability and its potential driving mechanisms in Central Asia.

2. Study Area

Sayram Lake (44°30′–44°42′ N, 81°05′–81°15′ E) lies in the Bortala Mongolian Autonomous Prefecture of Xinjiang, China. It is the highest-elevation and largest alpine closed-basin lake in the region. The lake surface is situated at an elevation of 2071 m above sea level, with a surface area of 453 km^2. The average water depth is 56 m, and the maximum depth reaches 99 m [31]. Sayram Lake occupies an alpine basin on the northwestern margin of the Tianshan Mountains and is surrounded by high mountains on all sides [32]. This enclosed setting strongly influences sediment transport and deposition, favoring the accumulation and preservation of aeolian material in the lake sediments.

Located in the interior of the Eurasian continent, Sayram Lake is influenced by the westerlies and characterized by a temperate continental semi-arid climate. The mean annual temperature is approximately 0.5 °C, and annual precipitation exceeds 350 mm, with the majority falling between May and September [33]. Westerly and northwesterly winds prevail year-round in the Sayram Lake region. The westerly circulation is the dominant mechanism for atmospheric moisture transport [34] and is also the main driving force for the long-distance transport of aeolian dust. The vegetation in the lake region and its surrounding areas exhibits vertical zonation. Alpine and montane meadows dominate the high-altitude and mountainous zones, while steppe and desert steppe vegetation types prevail in the lakeshore area [35]. Sparse vegetation cover and the semi-arid climate promote surface wind erosion, soil particle loosening, and further aeolian transport, making the study area an important potential source area of wind-blown material.

3. Materials and Methods

3.1. Coring and Radiocarbon Dating

In July 2009, a 300 cm-long sediment core (SLM2009) was retrieved from the central depositional basin of Sayram Lake at a water depth of 86.0 m, using an UWITEC floating platform equipped with a piston coring system (UWITEC, Mondsee, Austria) (Figure 1). The core was transported to the laboratory and subsampled at 1 cm intervals for subsequent

https://doi.org/10.3390/quat9020030

analyses. To establish the sedimentary chronology, accelerator mass spectrometry (AMS) ^{14}C dating was employed. A total of 16 samples collected at different depths in the core were dated to determine chronology. Dating analyses were performed by the AMS Laboratory of the University of Tokyo (Japan) and the Beta Analytic Radiocarbon Dating Laboratory in Miami (USA).

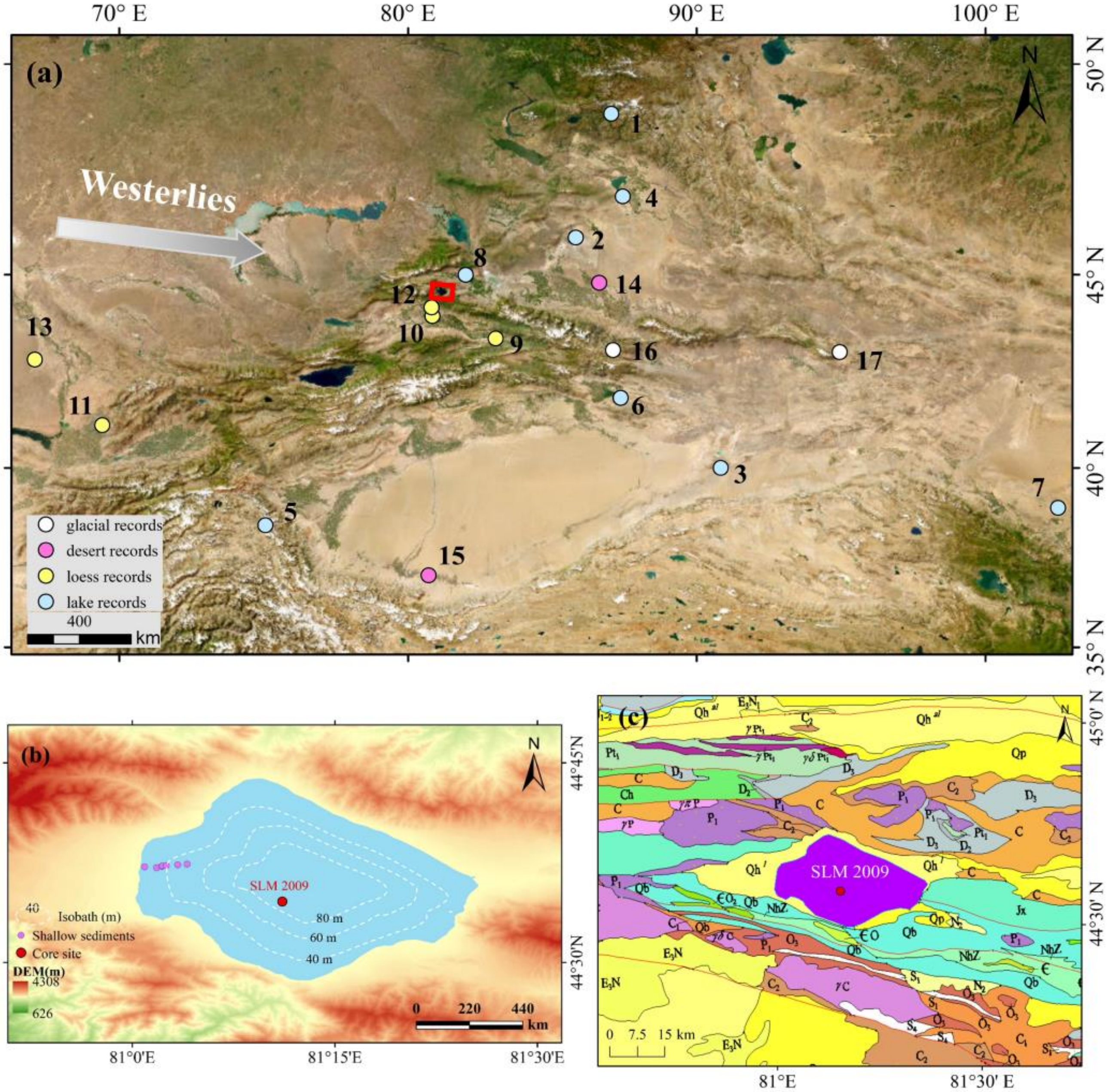

Figure 1. Location of sampling site and other aeolian records mentioned in the text. (**a**) Location of Sayram Lake (red rectangular area) and aeolian records referenced in the text in Central Asia: 1. Shuanghu Lake [16]; 2. Lake Ailike [22]; 3. Lop Nur [36]; 4. Jili Lake [37]; 5. Lake Karakul [38]; 6. Bosten Lake [39]; 7. Qingtu Lake [40]; 8. Ebinur Lake [41]; 9. 10 loess sections in Yili Basin [14]; 10. loess/sand sections in Yili Basin [15]; 11. The Karasu (KA) loess section [42]; 12. The Sangongxiang (SGX) loess profile [23]; 13. Shayan loess [24]; 14. sand dunes in Gurbantunggut Desert [43]; 15. Cele Oasis [44]; 16. Urumqi glacier no. 1 [45]; 17. Yushugou Glacier No. 6 [46]; (**b**) Location of core SLM2009 and seven shallow sediment samples; (**c**) Geological sketch map around Sayram Lake.

In addition, to verify the relationship between lake sedimentary dynamics and grain size distribution, seven sampling sites were established along a transect from the shoreline to the center of Sayram Lake in 2023, and seven shallow sediment samples were collected. The locations of these samples, together with core SLM2009, are shown in Figure 1.

3.2. Grain-Size Analysis

Samples were treated with 10 mL of 10% HCl to remove carbonates and with 10 mL of 30% H_2O_2 to oxidize organic matter. Sample pretreatment and measurement were conducted in accordance with the experimental protocol described in the reference [47,48]. After treatment, the sample was rinsed with deionized water until neutral. Then, 10 mL of 0.05 mol/L $(NaPO_3)_6$ solution was added, and the sample was oscillated in an ultrasonic cleaner for approximately 10 min. Finally, the grain size distribution was measured using a Malvern Mastersizer 2000 laser particle analyzer (Malvern Instruments Ltd., Malvern, UK) equipped with a Hydro MU wet dispersion unit. Each sample was measured in triplicate to ensure the analytical error was less than 3%.

3.3. End-Member Modeling Analysis

End-member modeling analysis (EMMA) decomposes the mixed signals embedded in sediment grain size data into several end-members (EMs) based on mathematical algorithms, including principal component analysis and least-squares optimization. Each end-member characterizes a specific sedimentary component with distinct grain size characteristics, typically corresponding to unique depositional processes or transport mechanisms. Consequently, this approach facilitates a more profound understanding of sediment provenance, hydrodynamic conditions, and the integrated paleoclimatic and paleoenvironmental signals [49–51]. Currently, EMMA has been widely applied in the research of loess, desert, rivers, and lacustrine sedimentary environments to reconstruct past environmental changes [13,17,22,52–56]. In this study, both parametric (Gen. Weibull distribution function) and non-parametric EMMA were conducted on the grain-size dataset from sediment core SLM2009 using the Analysize 1.2.2 software package [50], a MATLAB R2024a-based tool. The selection of the optimal number of end-members (EMs) was governed by several diagnostic indices and statistical criteria. These include (1) the linear correlation coefficient (R^2), which reflects the overall correlation between the modeled end members and the original dataset, with higher values indicating a better model fit and stronger representativeness of the extracted end members; (2) the end-member correlation (EM correlation), which describes the degree of similarity among the extracted end members, where higher values indicate greater overlap in their grain size distributions, reduced independence among end members, and a higher likelihood of overfitting; (3) the angular deviation, which measures the deviation between the modeled end-member curves and the original grain size distributions during shape fitting, with larger values indicating greater fitting errors caused by differences in end-member curve shapes; and (4) the selection criterion for the number of end members, in which the smallest possible number of components is chosen while still achieving satisfactory performance across the above indicators, thereby ensuring both a good model fit and reasonable model simplicity.

4. Results

4.1. Radiocarbon Dating

The chronological framework of the SLM2009 core was established using 16 AMS ^{14}C dating results on bulk organic matter (Table A1). To ensure the reliability of the age-depth model, three samples from depths below 245 cm at the core base were excluded. These samples exhibit anomalously positive $\delta^{13}C$ values (ranging from −21.9‰ to −18.2‰) and extremely low total organic carbon contents (TOC < 1%), which clearly indicate a shift in organic matter sources [34]. The excluded sample (Tka-15149) yielded a ^{14}C age of

(14,550 ± 60) a BP, with a calibrated calendar age range of 17,381~17,989 cal a BP [57]. As this interval predates the Holocene, removing these samples does not affect the primary objective of this study, which focuses on Holocene environmental evolution.

Based on the linear regression intercept of the 13 valid ^{14}C ages, a reservoir effect of 778 years was estimated for the lake and applied to correct all radiocarbon dates. Although reservoir ages in closed-basin lakes may vary through time and represent a potential source of chronological uncertainty, the estimated value of 778 years is consistent with reservoir effects reported for other closed-basin lakes in Xinjiang (e.g., 760 a for Wulungu Lake [58], 790 a for Balikun Lake [59]), confirming the reliability of this reservoir correction value. The age–depth model was constructed using the Bacon 3.2 software (Figure A1) [60]. The results indicate that the basal age of the core is approximately 12,780 cal a BP. Sedimentation rates range from 0.17 to 0.34 cm/a, with an average of 0.26 cm/a. The model produces a 2σ uncertainty envelope of ±0.2 cal ka. Compared with the millennial-scale environmental variability examined in this study, this chronological uncertainty is negligible and does not affect the main conclusions.

4.2. Results of Grain Size End-Member Analysis

The Analysize model developed by Paterson and Heslop [50] was applied to perform both parametric and non-parametric EMMA on the grain-size dataset from core SLM2009. Superior model fit is indicated by higher linear correlation coefficients (R^2), lower angular deviations, and end-member cross-correlation [54]. The non-parametric end-member modeling produced a linear coefficient of determination (R^2) of 0.9907, an angular deviation of 4.8179, and an inter-end-member correlation coefficient of 0.1281, whereas the corresponding values for the parametric end-member modeling were 0.9866, 5.7936, and 0.2365, respectively. Compared with the parametric approach, the non-parametric method yields a higher R^2 value, smaller angular deviation, and lower inter-end-member correlation. These results indicate that the non-parametric model achieves a better fit to the measured grain size data, with end-member grain size curves that more closely resemble the observed distributions. In addition, the extracted end members are more independent and exhibit clearer distinctions in their sedimentary dynamic significance. Therefore, the non-parametric method provides a more stable and reliable end-member decomposition and was selected in this study.

In applying non-parametric EMMA to SLM2009, several key parameters were considered. Generally, R^2 above 0.9, angular deviation less than 5°, and low end-member correlation are required, while following the principle of minimal end-member number [50,61,62]. When the number of end-members was 3, the R^2 was 0.976, but the angular deviation reached 7.8°, exceeding the 5° threshold. With 4 end-members, the R^2 increased to 0.991, angular deviation was reduced to 4.8°, and the end-member correlation was 0.108, indicating low mutual dependence and thus no overfitting. Although 5 end-members yielded a slightly higher R^2 of 0.996 and an angular deviation below 5°, the end-member correlation increased to 0.260, showing no significant improvement in model performance (Figure 2a,b). Considering all parameters and aiming for a parsimonious model, four end-members (EM1, EM2, EM3, and EM4) were ultimately selected for further analysis. The final modeling results are shown in Figure 2c,d. The specific R^2 values for each sample for the four end-members are provided in Table A2. A few samples exhibit relatively low R^2 values (<0.90), but these are still statistically acceptable for end-member modeling analysis. These likely reflect more complex grain-size distributions and mixed depositional processes in these intervals. Such deviations may be associated with short-term sedimentary perturbations or transitional depositional conditions, but they do not affect the overall robustness of the EMMA results.

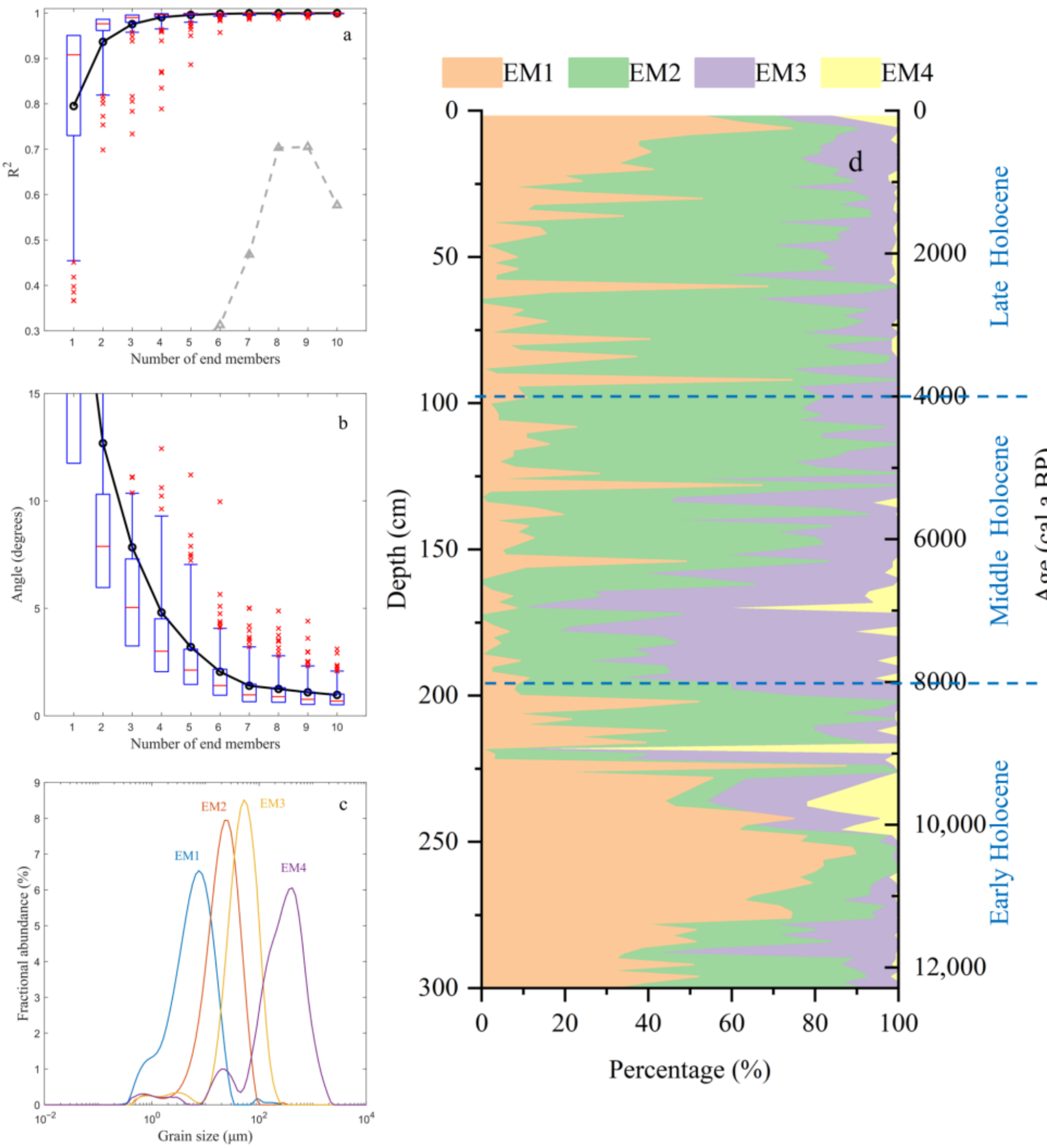

Figure 2. Grain-size end-member modeling results of core SLM2009. (**a**) Coefficient of determination (R^2); (**b**) Angular deviation; (**c**) Grain-size frequency distribution curves of the end-members; (**d**) Proportional contribution of EMs.

4.3. Characteristics of End-Member Compositions

The four end-members (EMs) identified from core SLM2009 have average contributions of 26.48%, 47.97%, 22.85%, and 2.69%, respectively. In this study, sediment grain sizes were classified following the Udden–Wentworth scale [63,64]. EM1 has a modal grain size of 7.58 µm and is classified as very fine silt. EM2 exhibits a modal grain size of 26.30 µm and consists primarily of medium silt. EM3, with a modal grain size of 52.48 µm, belongs to the coarse silt fraction. EM4 has a mode at 416.86 µm, classified as medium-grained sand (Figure 2c). As shown in Figure 2d, EM1 exhibits higher concentrations at approximately 0–470 cal a BP and 8450–12,280 cal a BP. EM2 is primarily distributed around 560–5580 cal a BP. EM3 shows a higher contribution from ~5860 to 7360 cal a BP. A marked increase in EM4 content is observed around 9060–9560 cal a BP. Overall, the sedimentary types of core SLM2009 from base to top exhibit the following vertical succession: the basal section is dominated by very fine silt, with an increase in medium-grained sand in the overlying basal interval; the middle section is characterized mainly by coarse silt, whereas the upper section is dominated by very fine to fine silt.

4.4. Shallow Sediment Grain Size Results

The shallow sediment samples collected in 2023, with water depths ranging from 11.7 m to 64.7 m, exhibit a decreasing mean grain size trend from nearshore to the lake center (Table 1). The grain size declined from 10.41 µm to 7.13 µm, while the median grain size decreased from 10.29 µm to 7.60 µm. All shallow samples exhibit highly negatively skewed distributions, with skewness values ranging from −0.32 to −0.57 [65]. The skewness becomes increasingly negative as water depth increases.

Table 1. Locations and grain size parameters of surface shallow samples in Sayram Lake.

Site No.	Offshore Distance (km)	Depth (m)	Mean Size (µm)	Median Size (µm)	Skewness
SLM23-01	0.42	11.7	10.41	10.29	−0.32
SLM23-02	1.47	29	9.80	10.07	−0.43
SLM23-03	1.91	35	9.16	9.34	−0.40
SLM23-04	1.96	35	9.12	9.42	−0.48
SLM23-05	2.3	41.2	9.40	9.87	−0.56
SLM23-06	3.32	54.5	7.43	8.00	−0.57
SLM23-07	4.14	64.7	7.13	7.60	−0.53

5. Discussion

5.1. Implication of End-Members in Sayram Lake

Grain size analysis of lake sediments enables the identification of climate-sensitive components and the recognition of sedimentary signals associated with extreme events such as storms [19] and earthquakes [66]. Due to potential mixing during sedimentation, grain-size distributions often exhibit multimodal characteristics [67]. Therefore, applying EMMA is essential for separating sediment components associated with different transport mechanisms.

Four end-members (EMs) were extracted, and their variations reflect changes in depositional conditions. EM1 has a modal grain size of 7.58 µm and a mean grain size of 5.8 µm, representing the finest fraction. Generally, particles smaller than 20 µm can be transported over long distances in high-altitude suspension and settle when wind strength decreases [68,69]. Such finest particles are easily affected by external factors and can even deposit by attaching to coarser particles [70]. Suspension sedimentation is thought to be the main depositing mechanism for the finest fraction [71]. The modal grain size of EM1 in this study is comparable to that of the suspended component EMs identified in Ailike Lake (5.1 µm) and Bosten Lake (7.29–9.3 µm) in northern Xinjiang [72,73]. Therefore, EM1 represents typical suspended material in lacustrine conditions and is mainly controlled by still-water deposits.

EM2 has a modal grain size of 26.30 µm, with a mean size of 19.06 µm, also classified as fine particles, slightly coarser than EM1, and is classified as medium suspension material [74] with relatively good sorting. In arid region lakes, river runoff typically cannot deliver coarse particles to the lake center but can transport finer particles into deeper areas, where they settle in low-energy environments [70,75]. During periods of increased precipitation or glacial meltwater, the lake level rises rapidly. The sampling site is located farther from the shoreline in the central basin, and weakened hydrodynamics lead to finer sediment grain sizes [32]. Similar sedimentary processes have been observed in arid lakes such as Ebinur Lake [73] and Ailike Lake [22] in Xinjiang. The seven shallow sediment samples collected in 2023 exhibit clear spatial variation. From the lake shore to the center, mean grain size generally decreases (Table 1). This modern sedimentary pattern suggests that the nearshore zone, influenced by river input and wave action, experiences stronger hydrodynamic conditions that favor the deposition of coarser particles. In contrast, the central part of the lake is characterized by weaker hydrodynamic forces, allowing finer particles to accumulate. These observations support the interpretation of EM2 as a proxy indicator for lake hydrodynamic intensity.

EM3 has a modal size of 52.48 μm, classified as coarse silt, primarily ranging from 20 to 90 μm. Its transport mechanism is mainly dominated by short-term suspension and/or modified saltation [69]. Coarse particles are primarily delivered into lake basins in arid and semi-arid areas by wind [37,76–78]. Furthermore, this grain size range is similar to that of surface loess samples from the Ili Basin in Xinjiang [23,79], indicating that the dust depositing into Sayram Lake should originate from nearby mountainous and loess deposits. EM4 shows a mode at 416.86 μm and a mean grain size of 230.37 μm, with a relatively wide grain size distribution, and belongs to the medium sand fraction. Generally, rivers in the Central ACA lack the capacity to transport such coarse sand into the center of a large lake [36]. These coarse grains are generally difficult to transport over long distances under normal wind power. However, during strong-wind events, dust storms may reach the lake center through saltation or suspension [70,80]. Therefore, EM3 + EM4 can serve as a proxy for regional aeolian activity.

The grain size characteristics of shallow sediments from Sayram Lake provide an important modern depositional analog for interpreting the depositional significance of grain size end-members (EMs) identified in the sediment core. Overall, the shallow sediments are dominated by fine-grained fractions, with mean grain sizes ranging from 7.13 to 10.41 μm and median grain sizes ranging from 7.60 to 10.29 μm, indicating that the depositional environment of the lake basin is generally characterized by low-energy, quiescent hydrodynamic conditions. Both mean and median grain sizes show a fining trend with increasing water depth, consistent with the typical hydrodynamic sorting effect in lacustrine systems, whereby coarser particles preferentially deposit in nearshore zones while finer particles are transported toward deeper parts of the basin [81]. All shallow samples exhibit negative skewness, indicating that the grain size distribution curves have a coarse tail. Negative skewness generally reflects the superimposition of a minor coarse-grained fraction on a background of fine-grained deposition [65,82]. Given that Sayram Lake is a closed alpine lake situated within the arid inland basin of the Westerlies, the presence of coarse particles in deep-water environments cannot be explained solely by low-energy suspension processes [83]. We interpret this coarse fraction as an indicator of aeolian input, likely derived from near-source saltation of sand particles or direct deposition during dust storm events. Furthermore, the slightly stronger negative skewness at deep-water sites suggests that a small proportion of coarse particles can traverse the lake basin and be deposited in the relatively low-energy central lake environment. This indicates that wind-transported coarse particles are not restricted to nearshore deposition, but could be delivered to the center of the lake basin and preserved in the sedimentary record. Consequently, the coarse-grained end-members identified in the sediment cores are unlikely to be controlled solely by internal lacustrine hydrodynamic sorting; rather, they likely record variations in aeolian input to the lake. Therefore, the grain size characteristics of modern shallow sediments provide a robust basis for interpreting the environmental significance of grain size end-members in the sediment core, supporting the use of coarse end-members (EM3 + EM4) as effective proxies for reconstructing the regional history of aeolian activity.

In studies of lake and terrestrial sediments across the ACA region, coarse-grained fractions have been widely recognized as effective proxies for aeolian activity. Multiple independent records (Figure 1) show a high degree of consistency in the indicative grain size intervals, supporting their strong regional applicability. In the Lop Nur sediments, coarse-grained fractions with grain sizes ≥ 300 μm serve as reliable indicators of aeolian activity [36]. By comparing grain size distribution patterns of sediments, modern aeolian dust samples, and shallow sediments, Qiang et al. [37] demonstrated that the 40–200 μm fraction constitutes the primary aeolian indicator in Jili Lake, northern Xinjiang. Sediment samples collected from the southern Gurbantunggut Desert showed that the coarse end-member components EM2 + EM3, with modal grain sizes of 178 μm and 283 μm, respectively, represent wind signals [43]. Similarly, in Lake Karakul of Central Asia, coarse grains > 64 μm directly reflect the frequency and intensity of sandstorm events [38]. While grain size components > 19.35 μm in the sediments of Bosten Lake, Xinjiang, have been demonstrated to capture variations in aeolian activity [39]. In addition, evidence from glacier snow samples in the Tianshan Mountains further corroborates the consistency of the aeolian grain size range. Dust layers from Glacier No. 6 in the Yushugou region are dominated by coarse mineral particles with grain sizes concentrated in 18.7–72.6 μm, indicative of strong aeolian events [46]. Glacial snow samples from the Urumqi Glacier in the eastern Tianshan similarly record pronounced coarse fractions (20–80 μm) during dust periods [45], a range that closely matches the EM3 grain size range identified in Sayram Lake.

Modern meteorological observations indicate that the Bortala Mongolian Autonomous Prefecture, where Sayram Lake is located, experiences frequent strong winds and dust events. The nearby Alashankou Pass is a well-known wind corridor in Xinjiang, with annual strong wind days (wind speed ≥ 17 m/s) reaching approximately 160–185 days [84]. In addition, floating dust events occur on average ~92 days per year in Bole City and ~112 days per year in Jinghe County near Sayram Lake [85]. Previous studies have shown that wind speed and the frequency of strong winds are key controlling factors influencing dust storm activities in Xinjiang [86]. Modern meteorological data demonstrate that strong winds in the study area can drive the saltation and short-term suspension of medium-grained sand particles, enabling the transport of coarse sediments to the central lake basin. Observational studies of modern aeolian deposits in the arid region of northwest China further show that coarse-grained fractions can occur in aeolian sediments under strong wind conditions. A coarse fraction of 250–600 μm was identified in near-surface atmospheric dust in the Cele Oasis [44]; the dominant grain size range of modern aeolian sediments in the playa of Ebinur Lake is 63–500 μm [41]; and coarse medium-grained sand particles were also detected in modern aeolian sediments at Qingtu Lake [40]. These findings confirm that coarse-grained particles in lake sediments of Central Asia are commonly associated with aeolian transport processes. The modern sedimentary records from these regional sites provide robust evidence for interpreting EM4 as a proxy for aeolian activity.

In addition to aeolian transport, processes such as ice rafting, turbidity currents, and slope failures may also transport coarse-grained particles into deep lake basins. Core SLM2009 is dominated by fine-grained sediments (mud, clay, and silt), with continuous lithological variation and no discernible event layers. Ice-rafted deposits are characterized by isolated coarse grains and poorly sorted deposits [87], which were not observed in the core. Turbidity currents generally form event layers characterized by graded bedding [88], whereas such turbidite structures are absent in the sediments. Slope failures usually produce chaotic deposits with mixed grain sizes and disturbed sedimentary fabrics [89], which are also not observed in the core. Alternative sources for the coarse fractions represented by EM3 and EM4 should also be considered. These components could potentially originate from hydrodynamic inputs associated with glacial meltwater, flood runoff, or enhanced precipitation, as their transport capacity is generally related to catchment hydrological intensity. Increased catchment humidity would also be expected to be reflected in pollen records. However, pollen records from the SLM2009 core indicate that although regional humidity during the middle Holocene was slightly higher than in the earlier period, hygrophilous and aquatic plants did not show a marked increase [57]. This pattern suggests that strong hydrodynamic processes were unlikely to have developed during this interval. These observations suggest that lake levels and runoff input did not increase substantially in the mid-Holocene. Accordingly, the possibility that the coarse fraction was directly transported to the lake center by flood runoff, intense precipitation, or glacial meltwater can be ruled out.

Based on multiple lines of evidence, including the presence of coarse-grained components in regional sedimentary records that match the grain size ranges of EM3 and EM4, modern meteorological conditions, and the favorable geomorphic setting of the lake basin, EM3 represents aeolian dust transported regionally by suspension, whereas EM4 mainly represents local aeolian materials transported by saltation under relatively strong wind conditions. Therefore, EM3 + EM4 can be collectively used as an effective proxy for the intensity of aeolian activity in the Sayram Lake basin.

5.2. Holocene Aeolian Activity and Its Relationship with Climate and Environmental Changes

Based on the established aeolian activity proxy (EM3 + EM4) and regional comparison data, this study reconstructs the Holocene evolution of aeolian activity in Sayram Lake. Dust sources in the region primarily include fluvial alluvial deposits, loess accumulations, weathered debris from Tianshan bedrock, and glacial erosion products. Since hydrothermal conditions regulate aeolian activity, considering the regional climate background provides a more comprehensive perspective for interpreting its dynamic mechanisms.

On the millennial scale, Holocene temperature changes in Central Asia exhibit a three-stage pattern: a cooler early Holocene (before 8.0 cal ka BP), a warmer middle Holocene (8.0–4.0 cal ka BP), and a cooling trend during the late Holocene (from 4.0 cal ka BP to present) (Figure 3e) [90]. In contrast, humidity reconstructions from five lakes in Xinjiang (Figure 3f) [91] indicate a trend of drier conditions during the early to middle Holocene and a gradual increase in moisture from the middle to late Holocene.

During the early Holocene (~12.0–8.0 cal ka BP), EM3 + EM4 values show distinct peaks at 11.7–11.2 cal ka BP and 9.2–8.1 cal ka BP (Figure 3a), with the peak around 8.5 cal ka BP, which may indicate a short-term intensification of aeolian activity. Overall, aeolian activity during this period was relatively strong but infrequent, likely due to arid environmental conditions that exposed large quantities of loose surface material, providing abundant sources for aeolian activity.

In the middle Holocene (8.0–4.0 cal ka BP), aeolian activity intensified significantly, particularly between 7.3 and 5.3 cal ka BP (Figure 3a). Although minor temporal discrepancies may arise from reservoir-age corrections, the 2σ uncertainty range of the Bacon age-depth model for the mid-Holocene interval of the SLM2009 core is approximately ±0.2 cal ka, and regional comparisons continue to support a consistent pattern of heightened aeolian processes. This is evident in the aeolian records from Ailike Lake (Figure 3c) [22], Barkol Lake [92], the Karasu loess section in Uzbekistan (Figure 3) [42], and Ca^{2+} concentrations from the Guliya ice core on the Tibetan Plateau (Figure 3d) [93]. Combined with climatic proxies, the mid-Holocene was characterized by high temperature and gradually increasing humidity (Figure 3e,f). This pattern is inconsistent with the speculation that warming may enhance vegetation coverage and that increasing humidity can improve soil erosion resistance, thereby weakening aeolian activity. This indicates that the linear changes in regional temperature and humidity do not entirely determine the intensity of aeolian activity.

In the late Holocene (from 4.0 cal ka BP to present), the intensity of aeolian activity decreased (Figure 3a), which may be related to regional cooling and increasing humidity. Lower temperatures suppress evaporation, while increased moisture enhances soil cohesion, thereby reducing susceptibility to wind erosion. However, it is noteworthy that despite improved moisture availability during the late Holocene, its inhibitory effect on aeolian activity was limited [15]. This phenomenon further confirms that there is no simple linear relationship between aeolian activity and temperature or humidity. According to variations in aeolian activity intensity in the Sayram Lake Basin since the Holocene, aeolian activity in this region does not follow a simple linear pattern in which higher humidity corresponds to weaker aeolian activity and higher temperature to stronger aeolian activity. Its response to changes in temperature and humidity is neither a simple positive correlation nor a simple negative correlation. This nonlinear characteristic provides regional-scale evidence for further investigation into the driving mechanisms of aeolian activity in Central Asia.

It should be clarified that the weakening trend in aeolian activity since the late Holocene reflects long-term environmental evolution at millennial to centennial timescales, which is not inconsistent with the recent intensification of dust storms. Increased dust storm activity in parts of the Northern Hemisphere represents short-term variability at interannual to decadal scales, driven by atmospheric circulation anomalies, regional moisture changes, and human activities, superimposed on the long-term weakening trend. Aeolian sediments are prone to mixing and shallow disturbance, making short-term signals from recent decades difficult to preserve. Moreover, the present sampling resolution does not allow identification of variability at 5–10-year timescales or rapid recent environmental changes. Thus, the absence of recent dust storm signals does not negate modern aeolian activity but results from differences in temporal scales and sedimentary recording mechanisms.

5.3. Global Comparison and Potential Driving Mechanisms of Aeolian Activity in Central Asia

Reconstructing regional aeolian activity and comparing it with global records can help clarify the potential mechanisms driving Holocene variations in aeolian activity. Aeolian processes are influenced by climate systems operating at multiple scales. At the global scale, atmospheric circulation and solar insolation exert significant influences. At the regional scale, local climatic conditions, topography, vegetation cover, and the availability of unconsolidated sediments may jointly regulate dust emission and deposition. The westerlies, the Siberian High, and the Caspian–Hindukush Index (CasHKI) are three key atmospheric systems that influence aeolian activity in Central Asia [42]. Therefore, comparing aeolian records from Sayram Lake with global records will help elucidate the mechanisms driving Holocene variations in aeolian activity.

Large amounts of dust originating from Central Asia can be transported over long distances through atmospheric circulation to remote regions such as the North Pacific and even Greenland, as documented by Greenland ice-core records [94,95]. The aeolian activity reconstructed from Sayram Lake (Figure 4a) shows similarities to variations in Ca^{2+} concentrations and dust mass accumulation rates measured in the Greenland Ice Sheet Project 2 (GISP2) ice core (Figure 4b) [96]. Both records generally indicate relatively strong aeolian activity in the early to middle Holocene and weaker activity in the late Holocene. Such correspondence implies that dust variability in Central Asia may have been linked to large-scale atmospheric circulation patterns operating across the Northern Hemisphere, rather than reflecting purely local processes. Furthermore, the aeolian activity represented by EM3 + EM4 exhibits similar temporal trends with North Atlantic ice-rafted debris (IRD) events (Figure 4c) [97] at the suborbital scale, implying a possible teleconnection between aeolian activity in the Sayram Lake basin and the North Atlantic climate system. A comparable long-term pattern is also observed between the reconstructed dust activity and the intensity of the Siberian High, inferred from K^+ concentrations in the GISP2 ice core (Figure 4d) [96], suggesting that the Siberian High may be an important atmospheric driver of aeolian activity in Central Asia. It should be noted that chronological uncertainties in age–depth models and potential differences in the response times of climate systems [98] may introduce temporal offsets of approximately 200–300 years between the Sayram Lake record and other global records. This offset generally falls within the combined chronological error ranges typically associated with lacustrine sediment records in arid Central Asia [34,99,100]. Nevertheless, the millennial-scale trends remain coherent, supporting the interpretation that large-scale changes in the Northern Hemisphere atmospheric circulation likely influenced aeolian activity in Central Asia.

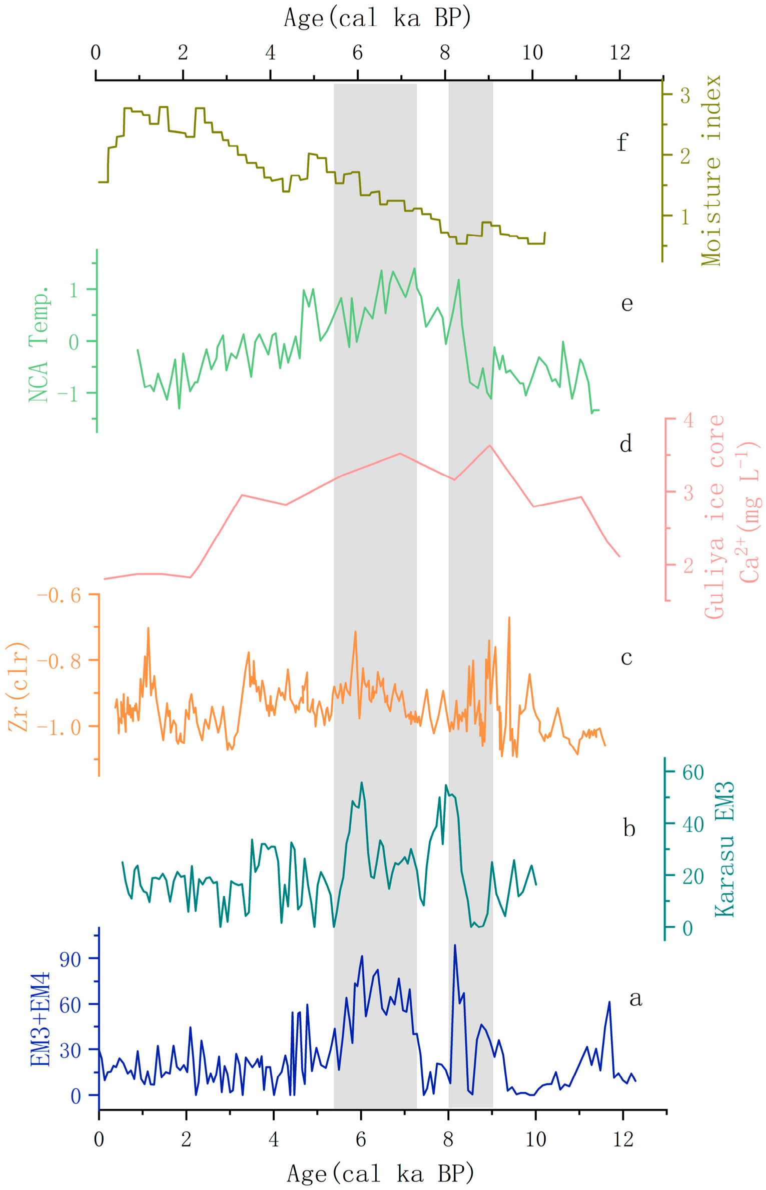

Figure 3. Comparison of other aeolian activity records and climate variability in the ACA region. (**a**) Reconstructed aeolian activity record based on EM3 + EM4 contributions from Sayram Lake; The chronological uncertainty (±0.2 ka) is smaller than the symbol size and is therefore not shown; (**b**) Aeolian activity proxy from the Karasu loess sequence [42]; (**c**) Aeolian activity record from the Ailike Lake (clr) profile [22]; (**d**) Ca^{2+} concentration from the Guliya ice core [93]; (**e**) Synthesized temperature reconstruction for northeastern Central Asia (NCA) [90]; (**f**) Regional average humidity index for Xinjiang [91].

Variations in winter solar insolation can significantly influence the intensity of the Siberian High. During the early and middle Holocene, winter insolation at high latitudes was relatively low (Figure 4g) [101]. This led to reduced winter temperatures across the Northern Hemisphere high latitudes, the cooling of polar air masses, and the further expansion of the Eurasian ice sheets (Figure 4f) [102,103]. These conditions collectively led to a significant strengthening of the Siberian High and drove the overall southward shift in the mid-latitude westerly circulation [95,104], providing a favorable atmospheric background for aeolian activity. As spring temperatures rose in the mid-latitudes, the convergence of cold polar air masses with warm, moist air masses, along with a steeper latitudinal temperature gradient, likely amplified cyclonic activity [105]. This, in turn, facilitated the development of high-velocity surface winds within the Sayram Lake basin, thereby intensifying aeolian activity. Meanwhile, the southward-shifted westerly belt failed to bring sufficient water vapor, leaving the study area in an arid condition. With low vegetation cover in the watershed, the extensive exposure of loose sediments provided an abundant source of material for aeolian activity, resulting in intense aeolian processes during the early Holocene.

During the middle Holocene, millennial-scale ice-rafted debris (IRD) cold events occurred frequently in the North Atlantic (Figure 4c), likely driven by high-latitude thermal gradients that promoted the southward expansion of polar air masses, in turn intensifying and expanding the Siberian High eastward and southward [22,106]. The strengthened Siberian High advected cold and dry air into inland Central Asia. On the one hand, the influx of cold, dry air likely resulted in dry, bare surfaces with low vegetation cover during winter and spring, creating wind-erosion-prone conditions. On the other hand, the southward expansion of the Siberian High enhanced cold air activity during winter and spring, increasing near-surface wind speeds in the arid Central Asian region and providing the necessary dynamics for dust emission and transport. Meanwhile, during the mid-Holocene, the North Atlantic Oscillation (NAO) was predominantly in a positive phase (Figure 4e; based on southern Alpine flood activity as an indirect proxy, with inherent uncertainty) [107]. Under these conditions, the pressure gradient between the Azores High and the Icelandic Low intensified, strengthening the North Atlantic westerlies, with increased wind speeds and a northward shift [90,108,109]. The intensified westerlies enhanced the capacity for long-distance dust transport, enabling dust from the desert regions of western Central Asia to be carried to the Sayram Lake basin [23]. At the same time, the northward displacement of the westerly belt likely diverted the Atlantic moisture transport pathways toward higher latitudes, thereby reducing moisture supply to Central Asia [110,111]. Such conditions may have produced dry, bare, and unstable surface soils with relatively low vegetation cover, thereby favoring dust emission. Therefore, aeolian activity during the mid-Holocene was jointly governed by the Siberian High and the westerly circulation. The Siberian High enhanced cold air outbreaks and near-surface wind fields, providing the dynamic conditions necessary for dust entrainment. In contrast, the strengthened westerlies facilitated transport processes, increasing the efficiency of dust delivery while simultaneously reducing moisture supply. Under this background, although regional humidity increased on long-term scales during the mid-Holocene, this signal primarily reflects summer hydrothermal conditions, whereas aeolian activity was mainly regulated by the intensity of winter and spring wind fields [110,111]. Consequently, the increase in summer humidity was insufficient to offset the dominant influence of strong winter–spring winds on aeolian activity, resulting in an asynchronous relationship between humidity variations and aeolian dynamics.

Under the influence of large-scale atmospheric circulation, regional surface conditions may have amplified aeolian activity. The relatively warm mid-Holocene climate likely triggered glacial retreat in the Tianshan Mountains [112] and enhanced meltwater runoff [113], leading to the accumulation of substantial unconsolidated sediments on alluvial fans and along the margins of the lake basin. Meanwhile, pollen records indicate generally limited vegetation cover in the catchment [57], rendering lacustrine sediments prone to exposure under seasonal arid conditions. These factors provided the necessary material basis for aeolian activity; however, their role was primarily to amplify the sedimentary response rather than to drive the regional-scale intensification of aeolian processes. In summary, the enhanced aeolian activity recorded at Sayram Lake during the mid-Holocene can be attributed to coupled changes in mid- to high–latitude atmospheric circulation in the Northern Hemisphere. The strengthened Siberian High supplied cold air and strong wind forcing, while the intensified westerlies enhanced dust transport capacity and limited moisture input. Together, these processes created a climatic background conducive to increased aeolian activity.

In contrast, winter insolation increased during the late Holocene (Figure 4g) and the Eurasian ice sheet declined (Figure 4f). Arctic warming reduced the extent of polar cold air masses, accompanied by a weakened Siberian High [114,115], resulting in decreased near-surface wind speeds. At the same time, the NAO entered a negative phase, and the Siberian High also moved westward, resulting in increasingly stable air masses over Central Asia and an enhanced impact of the westerlies in the mid-latitudes [116]. Higher temperatures at high latitudes likely increased marine evaporation, thereby increasing moisture flux into Central Asia via the Westerlies. This rise in regional relative humidity led to significant changes in vegetation and soil characteristics. Artemisia/Chenopodiaceae (A/C) ratios and Pollen records from Ulungur Lake [58] and Sayram Lake [57] in northeastern Central Asia indicate a shift from desert-steppe to grassland vegetation, reducing the extent of the Gobi deserts. This ecological transition, driven by greater vegetation cover and higher soil moisture under the strengthened influence of the westerlies, likely suppressed dust emissions and led to a marked decline in aeolian activity.

Previous studies have yielded contrasting insights into the evolutionary characteristics and driving mechanisms of Holocene aeolian activity. Some records indicate intensified aeolian activity during the late Holocene, commonly attributed to increased regional sediment supply and the influence of human activities [15] or linked to the intensification of the westerlies [16]. Other studies suggest that the reduction in aeolian activity during the mid-Holocene resulted from the combined effects of a strengthened summer monsoon and adjustments in the Westerlies [13,23]. In contrast, the Sayram Lake record reveals relatively strong aeolian activity in the middle Holocene, followed by a decline in the late Holocene. In this study, we emphasize the dominant role of the large-scale atmospheric circulation in the Northern Hemisphere. Specifically, variations in the intensity of the Siberian High provide the dynamic forcing for aeolian entrainment, while the westerlies modulate the efficiency of dust transport and regional moisture supply. The synergistic interaction between these two systems governs the overall evolutionary trend of aeolian activity, whereas local surface conditions amplify the sedimentary response to aeolian processes. We propose that the discrepancies among different records likely reflect variations in proxy sensitivity [117], regional setting, and the relative contributions of geomorphic processes versus large-scale atmospheric circulation. Although grain size end-member analysis provides a reliable proxy for regional aeolian activity, independent mineralogical validation (e.g., XRD, SEM) of the aeolian origin of sediments was not performed in this study. Future work incorporating such analyses will further strengthen interpretations of sediment provenance and transport mechanisms.

https://doi.org/10.3390/quat9020030

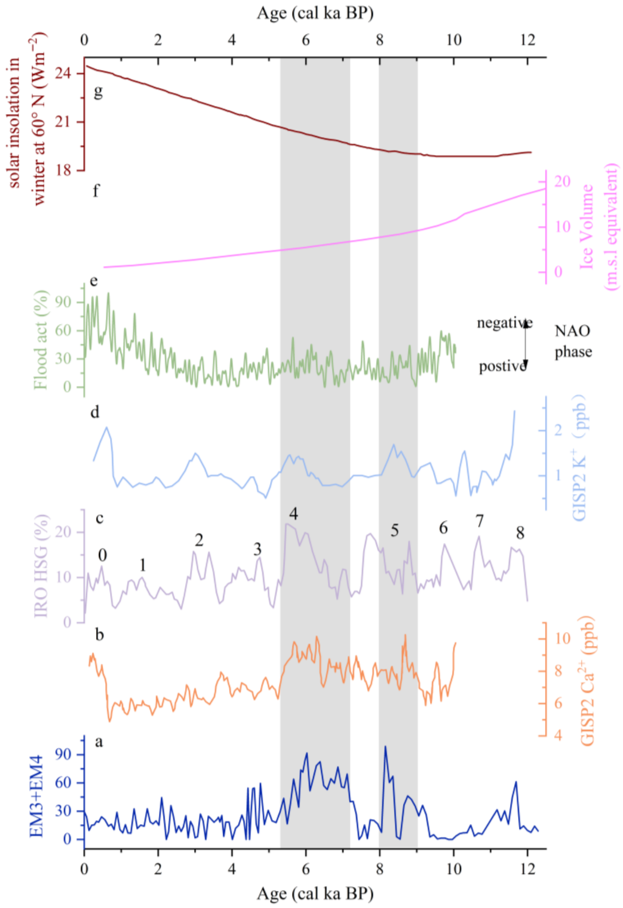

Figure 4. Comparison of Holocene aeolian activity at Sayram Lake with global records and potential driving mechanisms. (**a**) Reconstructed aeolian activity based on EM3 + EM4 contributions from Sayram Lake; (**b**) Ca^{2+} concentration from the GISP2 ice core, representing dust flux in Greenland [96]; (**c**) North Atlantic ice-rafted debris (IRD) record [97]. Numbers indicate the timing of the eight Bond events; (**d**) K^{+} concentration from the GISP2 ice core, serving as a proxy for the strength of the Siberian High [96]; (**e**) Holocene North Atlantic Oscillation (NAO) reconstruction based on southern Alpine flood activity [107]; (**f**) Ice volume of the Eurasian Ice Sheet [102]; (**g**) Winter insolation at 60° N latitude [101].

6. Conclusions

Grain-size end-member analysis indicated that the coarse-grained fraction (EM3 + EM4) provided a reliable proxy for aeolian activity intensity in the Sayram Lake basin, reflecting variations in wind-driven coarse particle input. The reconstructed record shows that aeolian activity was relatively strong during the early and mid-Holocene and gradually weakened during the late Holocene. This study suggests that the evolution of aeolian activity in Lake Sayram during the Holocene was closely linked to variations in the Siberian High and the westerly circulation, highlighting the high sensitivity of regional aeolian activity to large-scale atmospheric circulation changes in the Northern Hemisphere. The Siberian High controlled aeolian entrainment by modulating cold air outbreaks and near-surface wind fields during winter and spring. Meanwhile, the westerlies regulated the efficiency of long-distance dust transport and deposition. The synergistic interaction between these two circulation systems constitutes the mechanism regulating the evolutionary dynamics of aeolian activity in the arid Central Asian region.

Author Contributions: Conceptualization, S.Y., L.C., D.N., D.W. and Q.J.; methodology, S.Y., Y.X. and Q.J.; software, Y.X. and Q.J.; validation, L.C., D.N., D.W. and Q.J.; formal analysis, S.Y., L.C., D.N. and

D.W.; investigation, L.C., D.N., D.W. and Q.J.; resources, Y.X., L.C., D.N., D.W. and Q.J.; data curation, S.Y., L.C., D.N. and D.W.; writing—original draft preparation, S.Y.; writing—review and editing, Y.X. and Q.J.; visualization, S.Y., Y.X. and Q.J.; supervision, Q.J.; project administration, Q.J.; funding acquisition, Q.J. All authors have read and agreed to the published version of the manuscript.

Funding: This study was supported by the National Natural Science Foundation of China (Grant Nos. 41672349 and 40802084).

Data Availability Statement: Data will be made available on request.

Acknowledgments: We thank anonymous reviewers and editors for their valuable comments and suggestions.

Conflicts of Interest: The authors declare that they have no known competing financial interests or personal relationships that could have appeared to influence the work reported in this paper.

Abbreviations

The following abbreviations are used in this manuscript:

ACA	Arid Central Asia
EMMA	End-member modeling analysis
EM	End-member
IRD	Ice-rafted debris
CasHKI	Linear dichroism
GISP2	Greenland Ice Sheet Project 2
NAO	North Atlantic Oscillation

Appendix A

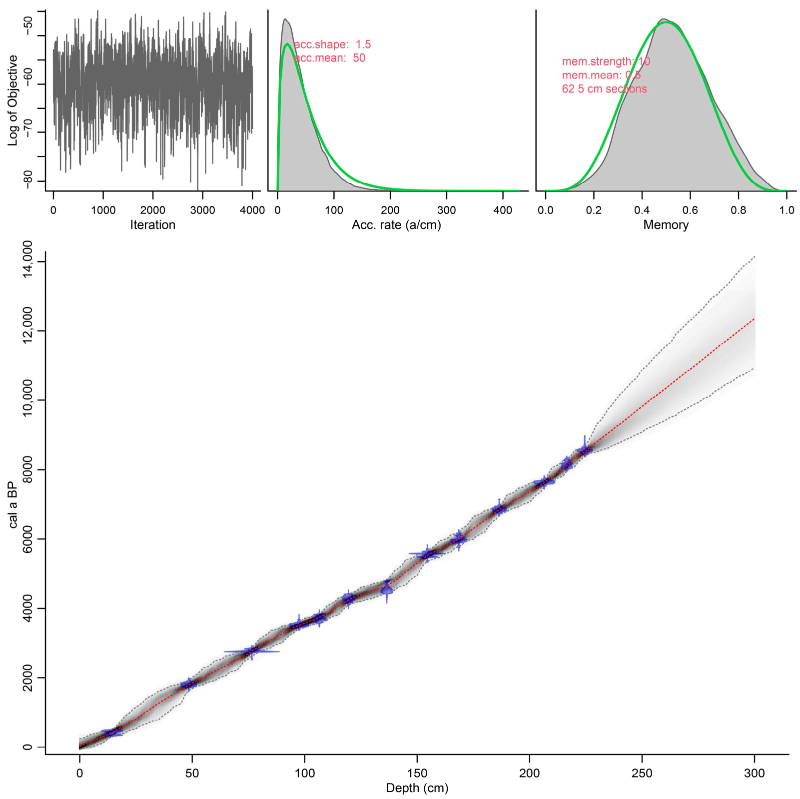

Figure A1. Age-depth model of core SLM2009 from Lake Sayram.

Table A1. ^{14}C dates and calibrated ages from core SLM2009 at Lake Sayram.

Lab ID	Depth (cm)	^{14}C Age (a BP)	$\delta^{13}C$ (‰)	C/N	Reservoir Corrected (−778 a)	Calendar Age (cal a BP)
Tka-15142	14.5	1150 ± 25	−25.7	13.4	372	426–501 (464)
Tka-15163	48.5	2670 ± 35	−26.3	14.9	1892	1727–1899 (1813)
Tka-15143	76.5	3425 ± 30	−27.6	14.0	2647	2739–2796 (2768)
Beta-469443	97.5	4080 ± 30	−27.1	15.4	3302	3454–3593 (3524)
Tka-15144	106.5	4215 ± 35	−29.6	18.1	3437	3608–3780 (3694)
Beta-469444	119.5	4640 ± 30	−26.5	13.7	3862	4225–4411 (4318)
Tka-15164	136.5	4815 ± 45	−28.9	12.9	4037	4416–4629 (4523)
Tka-15145	154.5	5625 ± 35	−28.7	15.4	4847	5578–5651 (5615)
Tka-15165	168.5	5980 ± 45	−25.4	17.2	5202	5893–6029 (5961)
Tka-15146	186.5	6795 ± 35	−26.8	12.0	6017	6776–6949 (6863)
Tka-15147	206.5	7555 ± 40	−28.0	10.5	6777	7577–7677 (7627)
Tka-15166	216.5	8120 ± 50	−25.2	14.6	7342	8021–8220 (8121)
Tka-15148	224.5	8560 ± 45	−26.7	10.3	7782	8455–8639 (8542)
Tka-15149	244.5	14,550 ± 60	−18.2	4.2	/	/
Beta-469445	257.5	16,010 ± 40	−20.4	3.8	/	/
Beta-469446	287.5	19,530 ± 60	−21.9	0.2	/	/

Table A2. The specific R^2 values for each sample for the four end-members.

Specimen	R^2	Theta	EM 1	EM 2	EM 3	EM 4
1	0.98925	4.73197	53.31746	17.08358	13.76157	15.83738
3	0.99265	3.94945	61.7819	13.59511	16.92003	7.70296
5	0.99133	4.63489	73.97279	16.12961	9.8976	0
7	0.99652	2.85634	49.74324	34.28489	15.17795	0.79392
9	0.99761	2.38542	37.35475	46.03876	14.41958	2.18692
11	0.99349	3.90889	37.25681	41.98332	20.75987	0
13	0.98409	6.1666	40.42899	39.69958	19.87144	0
15	0.98152	6.5833	36.5147	37.76271	25.1049	0.61769
17	0.98423	6.27143	32.16155	45.25835	22.5801	0
19	0.99482	3.57171	40.91317	43.78628	15.30055	0
21	0.99825	2.07625	18.42001	63.92288	14.94049	2.71662
23	0.99674	2.82819	23.7834	64.82276	8.86447	2.52937
25	0.99846	1.98412	6.0835	62.72812	30.9088	0.27958
27	0.9985	1.92383	22.68806	65.6282	10.41478	1.26896
29	0.98304	6.37612	52.41184	40.1048	6.94079	0.54257
31	0.99845	1.97877	12.40193	70.40874	16.00544	1.18389
33	0.99754	2.52084	10.41344	81.48858	6.68367	1.41431
35	0.9936	3.98953	33.68578	58.77208	7.54214	0
37	0.99926	1.38482	0	64.87618	34.48529	0.63853
39	0.99847	1.96744	13.72902	73.38384	11.45677	1.43037
41	0.9995	1.11734	15.28932	68.00945	15.70834	0.9929
43	0.99956	1.06431	8.20911	75.98284	15.2505	0.55756
45	0.99681	2.87563	0.59105	64.17307	34.16775	1.06812
47	0.99886	1.71596	4.7652	74.74585	18.71129	1.77766
49	0.99908	1.53042	8.42165	73.47009	16.60056	1.5077

https://doi.org/10.3390/quat9020030

Table A2. *Cont.*

Specimen	R^2	Theta	EM 1	EM 2	EM 3	EM 4
51	0.99719	2.70309	2.19516	76.10048	19.92593	1.77843
53	0.99904	1.56997	8.62083	74.62675	15.55315	1.19928
55	0.99178	4.58796	3.54746	48.77299	46.73219	0.94737
57	0.99885	1.71955	3.31178	70.49557	23.63541	2.55724
59	0.9612	10.64646	67.92589	32.07411	0	0
61	0.99962	0.97782	16.3436	74.29014	8.83359	0.53267
63	0.99345	4.13674	0	61.13652	38.86348	0
65	0.99332	4.19739	0	73.12028	26.87972	0
67	0.99827	2.12084	9.70726	81.58043	8.71231	0
69	0.99738	2.60676	6.21836	77.73984	16.04181	0
71	0.99954	1.07923	15.53511	74.74183	8.81442	0.90863
73	0.99862	1.88073	7.88115	77.00383	13.39211	1.72291
75	0.99516	3.55944	0.94488	71.47672	27.5784	0
77	0.99303	4.13459	39.86681	57.98157	0.27801	1.87361
79	0.99807	2.22708	5.96674	73.03159	19.32579	1.67589
81	0.9989	1.67816	9.34164	75.14844	13.76249	1.74743
83	0.98711	5.67303	36.64822	61.05437	1.66957	0.62784
85	0.99802	2.25394	17.81262	78.21886	3.96852	0
87	0.98906	5.41898	0	70.48058	29.51942	0
89	0.9939	3.99098	3.63011	74.40156	21.96833	0
91	0.97513	8.42523	73.79949	26.20051	0	0
93	0.99601	3.1902	8.30972	64.83358	26.8567	0
95	0.99604	3.18591	9.23649	67.10011	23.6634	0
97	0.99899	1.61051	10.68515	69.19129	20.12356	0
99	0.99256	4.41792	1.86525	74.65441	23.48034	0
101	0.99536	3.47675	3.10634	70.98007	25.91359	0
103	0.99247	4.43952	3.9036	75.51144	20.58496	0
105	0.99321	4.20261	3.78225	68.43455	27.7832	0
107	0.99662	2.92852	22.39677	73.50897	3.56013	0.53413
109	0.99949	1.14377	10.50346	69.26833	20.10008	0.12813
111	0.99949	1.14377	10.50346	69.26833	20.10008	0.12813
113	0.99882	1.7598	15.80557	84.19443	0	0
115	0.99707	2.76204	7.26405	79.30862	13.42734	0
117	0.99689	2.83633	7.36495	75.5807	17.05436	0
119	0.99537	3.46841	3.85164	67.86783	28.28053	0
121	0.99706	2.75107	8.13875	70.63809	21.22317	0
123	0.99338	4.12251	27.79081	72.20919	0	0
125	0.9968	2.95849	0	41.64312	58.35688	0
127	0.98291	6.75084	66.75963	33.24037	0	0
129	0.99256	4.40845	2.14494	67.29986	30.5552	0
131	0.99634	3.09785	0.09882	42.26312	57.63806	0
133	0.99183	4.54049	1.37965	40.79654	50.52297	7.30083

Table A2. *Cont.*

Specimen	R^2	Theta	EM 1	EM 2	EM 3	EM 4
135	0.99946	1.1708	13.16753	68.40996	18.42252	0
137	0.99946	1.16355	19.36294	72.51185	7.3203	0.80491
139	0.99849	2.00986	2.31157	34.0179	63.67053	0
141	0.99875	1.79791	11.09291	71.26332	17.64377	0
143	0.99633	3.05956	8.32025	58.25732	33.42243	0
145	0.9993	1.33487	12.39639	65.94701	21.6566	0
147	0.99699	2.79188	8.62539	71.51115	19.86346	0
149	0.99649	3.01983	4.94301	62.92659	32.1304	0
151	0.99847	1.98943	5.92758	47.31366	46.75877	0
153	0.96931	8.55712	48.69909	33.72674	15.92075	1.65342
155	0.99533	3.41266	10.7039	47.87855	39.75852	1.65903
157	0.9982	2.14477	5.24422	26.83718	64.08124	3.83736
159	0.99222	4.5485	0	49.09691	50.90309	0
161	0.99732	2.6345	0	62.9331	35.90942	1.15748
163	0.9908	4.85317	2.63207	19.51917	70.44536	7.4034
165	0.97455	7.99629	7.53474	17.08095	66.77625	8.60806
167	0.99078	4.90183	3.66336	8.0631	81.71613	6.55741
169	0.86689	17.77966	7.26841	0	45.47733	47.25426
171	0.99554	3.50426	0	44.60097	55.39903	0
173	0.99797	2.44099	0	31.62297	68.37703	0
175	0.99686	2.90704	3.1547	13.70112	83.14418	0
177	0.9624	9.76525	6.69644	6.66869	74.20602	12.42885
179	0.99528	3.53884	2.67	36.30095	61.02905	0
181	0.99839	2.06652	4.78343	38.61829	56.59827	0
183	0.99939	1.27476	2.26988	28.98474	68.74538	0
185	0.99854	2.03167	0	36.23658	63.76342	0
187	0.97841	7.41447	9.40673	9.51026	74.86351	6.2195
189	0.99561	3.41047	2.65983	37.6385	59.70166	0
191	0.99567	3.3973	2.52693	38.7555	58.71757	0
193	0.9573	10.35257	11.34591	15.40133	66.26675	6.98601
195	0.99617	3.12593	8.35826	48.59912	43.04261	0
197	0.99715	2.71945	7.73962	48.94025	43.32013	0
199	0.99945	1.18271	9.37354	61.72437	28.34136	0.56073
201	0.97785	7.69595	51.49534	48.50466	0	0
203	0.98206	6.70318	34.08259	61.09915	4.79082	0.02745
205	0.99926	1.38338	6.39645	76.60699	16.03607	0.96049
207	0.98695	5.79336	21.14131	77.53762	0.25223	1.06883
209	0.99974	0.80841	8.34797	68.87132	22.51884	0.26187
211	0.99024	4.65355	43.97611	35.04805	14.81134	6.16451
213	0.99313	4.14293	21.1053	60.93433	17.96036	0
215	0.98324	6.49209	39.10603	52.46889	8.42508	0
217	0.93587	12.74893	0	1.41296	0	98.58704

Table A2. *Cont.*

Specimen	R^2	Theta	EM 1	EM 2	EM 3	EM 4
219	0.99696	2.79646	3.26599	32.44771	62.88708	1.39922
221	0.99935	1.29011	3.11053	25.74912	67.4059	3.73445
223	0.99192	4.47127	86.78618	10.54792	1.43274	1.23316
225	0.99755	2.52822	13.35758	86.03751	0	0.60491
227	0.98096	6.29279	55.20249	6.65714	32.80645	5.33392
235	0.98133	5.79895	43.3868	9.23339	25.16891	22.2109
237	0.9686	7.61233	46.13978	10.46781	21.05099	22.34142
239	0.7895	20.93114	64.12869	0	21.01798	14.85333
241	0.87177	17.01466	74.42981	0	20.76484	4.80535
243	0.83561	18.50619	62.90624	0	26.32716	10.7666
245	0.982	6.05962	60.7447	12.58557	11.87073	14.799
247	0.99801	2.20299	77.39218	20.05743	0.86233	1.68805
249	0.99952	1.06933	75.3831	19.51524	4.87594	0.22572
251	0.99626	3.09099	88.3178	11.49448	0.18771	0
253	0.99693	2.76232	89.17595	9.73555	1.08851	0
255	0.99715	2.64418	81.05283	17.71593	0.77719	0.45406
257	0.99556	3.45243	81.31213	18.68787	0	0
259	0.99878	1.84743	79.23181	20.76819	0	0
261	0.99817	2.09276	75.1689	21.2009	1.05046	2.57975
263	0.99341	3.9814	78.71193	15.05688	5.41378	0.81742
265	0.99724	2.61341	72.55131	20.22324	7.22545	0
267	0.99831	1.98671	65.03464	27.56322	6.31753	1.08461
269	0.99744	2.40837	62.05304	22.0786	15.05604	0.81232
271	0.99706	2.72555	70.98824	25.45089	3.56087	0
273	0.99772	2.34529	73.91686	19.13724	6.9459	0
275	0.99635	2.94728	73.54677	20.71502	5.01286	0.72535
277	0.99433	3.65015	37.39733	29.12014	33.48253	0
279	0.99827	2.04189	51.17373	27.76875	21.05753	0
281	0.99839	1.87989	44.97151	22.91144	30.91621	1.20083
283	0.99574	3.22028	51.07624	31.65899	17.26478	0
285	0.99877	1.72863	38.53067	14.31304	47.15629	0
287	0.99289	4.04853	33.91958	1.32802	63.74258	1.00982
289	0.99862	1.82394	31.79134	55.9331	11.48565	0.78992
291	0.97532	7.52899	50.4841	34.26756	13.36945	1.87889
293	0.99855	1.88704	28.72936	60.45079	10.81986	0
295	0.97669	7.3979	51.61605	40.39554	5.74413	2.24428
297	0.99518	3.36881	39.11281	45.54191	15.34529	0
299	0.99921	1.38531	29.9557	59.98627	9.59692	0.46112

References

1. Ravasio, C.; Cremonesi, L.; Artoni, C.; Delmonte, B.; Maggi, V.; Potenza, M.A.C. Optical Characterization of Mineral Dust from the EAIIST Project with Digital Holography. *ACS Earth Space Chem.* **2021**, *5*, 2855–2864. [CrossRef]
2. Jäkel, E.; Becker, S.; Sperzel, T.R.; Niehaus, H.; Spreen, G.; Tao, R.; Nicolaus, M.; Dorn, W.; Rinke, A.; Brauchle, J.; et al. Observations and Modeling of Areal Surface Albedo and Surface Types in the Arctic. *Cryosphere* **2024**, *18*, 1185–1205. [CrossRef]
3. Rea, D.K.; Snoeckx, H.; Joseph, L.H. Late Cenozoic Eolian Deposition in the North Pacific: Asian Drying, Tibetan Uplift, and Cooling of the Northern Hemisphere. *Paleoceanography* **1998**, *13*, 215–224. [CrossRef]
4. Bailey, I.; Liu, Q.; Swann, G.E.A.; Jiang, Z.; Sun, Y.; Zhao, X.; Roberts, A.P. Iron Fertilisation and Biogeochemical Cycles in the Sub-Arctic Northwest Pacific during the Late Pliocene Intensification of Northern Hemisphere Glaciation. *Earth Planet. Sci. Lett.* **2011**, *307*, 253–265. [CrossRef]
5. Mahowald, N. Aerosol Indirect Effect on Biogeochemical Cycles and Climate. *Science* **2011**, *334*, 794–796. [CrossRef]
6. Chen, S.; Liu, J.; Wang, X.; Zhao, S.; Chen, J.; Qiang, M.; Liu, B.; Xu, Q.; Xia, D.; Chen, F. Holocene Dust Storm Variations over Northern China: Transition from a Natural Forcing to an Anthropogenic Forcing. *Sci. Bull.* **2021**, *66*, 2516–2527. [CrossRef]
7. Lu, H.; Zhao, C.; Mason, J.; Yi, S.; Zhao, H.; Zhou, Y.; Ji, J.; Swinehart, J.; Wang, C. Holocene Climatic Changes Revealed by Aeolian Deposits from the Qinghai Lake Area (Northeastern Qinghai-Tibetan Plateau) and Possible Forcing Mechanisms. *Holocene* **2011**, *21*, 297–304. [CrossRef]
8. Liu, B.; Jin, H.; Zhao, H.; Jin, J.; Sun, A.; Wang, X.; Zhang, X.; Ge, J.; Xu, Y.; Liu, J. End-Member Analysis of the Grain Size of Surface Sediments Used to Synthesize Holocene Aeolian Activity across the Ordos Plateau in Northern China. *Geoderma* **2025**, *460*, 117400. [CrossRef]
9. Yang, S.; Liu, X.; Cheng, T.; Luo, Y.; Li, Q.; Liu, L.; Chen, Z. Stepwise Weakening of Aeolian Activities During the Holocene in the Gannan Region, Eastern Tibetan Plateau. *Front. Earth Sci.* **2021**, *9*, 686677. [CrossRef]
10. Jia, F.; Lu, R.; Gao, S.; Li, J.; Liu, X. Holocene Aeolian Activities in the Southeastern Mu Us Desert, China. *Aeolian Res.* **2015**, *19*, 267–274. [CrossRef]
11. Cheng, L. Pronounced Changes in Paleo-Wind Direction and Dust Sources during MIS3b Recorded in the Tacheng Loess, Northwest China. *Quat. Int.* **2019**, *552*, 122–134. [CrossRef]
12. Xu, C.; E, C.; Shi, Y.; Zhang, J.; Sun, M.; Zhang, Z.; Zeng, Y. Holocene Aeolian Activity Recorded by Mountain Paleosols, Gonghe Basin, Northeast Qinghai-Tibet Plateau. *Front. Earth Sci.* **2022**, *10*, 832993. [CrossRef]
13. Liu, B.; Zhao, Y.; Liang, A.; Sun, A.; Zhang, Z.; Ge, J.; Zhao, H.; Chen, F. Quantitative Contributions of Different Atmospheric Circulation Systems to Holocene Aeolian Activity in Northwestern China: Evidence from a Closed Interdune Lake in the Tengger Desert Hinterland. *Glob. Planet. Change* **2024**, *243*, 104621. [CrossRef]
14. Kang, S.; Wang, X.; Wang, N.; Song, Y.; Liu, W.; Wang, D.; Peng, J. Siberian High Modulated Suborbital-Scale Dust Accumulation Changes Over the Past 30 Ka in the Eastern Yili Basin, Central Asia. *Paleoceanog. Paleoclimatol.* **2022**, *37*, e2021PA004360. [CrossRef]
15. Fan, Y. Increased Late Holocene Dust Activity Revealed by Loess Accumulation Rates in Central Asia. *Glob. Planet. Change* **2024**, *236*, 104416. [CrossRef]
16. Wang, H. Holocene Dust Activity in Inland Asia Driven by Both the Mid-Latitude Westerlies and the East Asian Winter Monsoon. *Glob. Planet. Change* **2025**, *245*, 104661. [CrossRef]
17. Yang, J.; Wang, H.; Gao, F.; Wang, Z.; Wang, S.; Fan, Y.; Li, T.; Liu, X.; Qu, W.; Li, J.; et al. Holocene Forcing of Aeolian Dust Activity over the Tibetan Plateau and Its Surroundings. *Glob. Planet. Change* **2024**, *235*, 104400. [CrossRef]
18. Li, Y. Positive Correlation between Dust Activity and Humidity in Arid Central Asia during the Holocene. *Quat. Sci. Rev.* **2024**, *324*, 108442. [CrossRef]
19. Li, W.; Ye, C.; Hu, H.; Li, G. Aeolian Activities Change and Possible Mechanisms in Central Asia on Sub-Orbital to Decadal Timescales. *Quat. Int.* **2023**, *672*, 30–42. [CrossRef]
20. Chen, S.; Liu, J.; Ma, S.; Fan, Y.; Jia, J.; Chen, J.; Chen, F. Holocene Dust Storm Variations across Northern Monsoonal Asia and Arid Central Asia: Contrasting Impacts of Climate Change. *Glob. Planet. Change* **2024**, *240*, 104524. [CrossRef]
21. Wei, H.; Song, Y.; Wang, Y.; Zhang, M.; Gholami, H.; Kang, S.; Li, Y.; Shukurov, S.; Shukurov, N.; Orozbaev, R. Variations in Central Asian Dust Activity and Potential Driving Mechanisms over the Past 80 Kyr. *Gondwana Res.* **2025**, *144*, 77–86. [CrossRef]
22. Chen, Y.; Liu, X.; Li, J.; Liu, X.; Ou, X. Impact of Millennial-Scale Fluctuations of the Siberian High on Holocene Aeolian Activity: Insights from Lake Ailike in Arid Central Asia. *Glob. Planet. Change* **2024**, *242*, 104593. [CrossRef]
23. Sun, H.; Song, Y.; Chen, X.; Cheng, L.; Liu, H. Holocene Dust Deposition in the Ili Basin and Its Implications for Climate Variations in Westerlies-Dominated Central Asia. *Palaeogeogr. Palaeoclimatol. Palaeoecol.* **2020**, *550*, 109731. [CrossRef]
24. Su, C.; Xu, Z.; Zhang, D.; Liu, Q.; Liu, J. Aeolian Dust History since 14.4 Cal. Ka B. P. Indicated by Grain-Size End Members of Shayan Loess in the Southern Kazakhstan. *Quat. Sci.* **2023**, *43*, 46–56. [CrossRef]
25. Wang, S.; Zhang, Z. New Progress of Lake Sediments and Environmental Changes Research in China. *Chin. Sci. Bull.* **1999**, *44*, 1744–1754. [CrossRef]

26. Tarasov, P.E.; Demske, D.; Leipe, C.; Long, T.; Müller, S.; Hoelzmann, P.; Wagner, M. An 8500-Year Palynological Record of Vegetation, Climate Change and Human Activity in the Bosten Lake Region of Northwest China. *Palaeogeogr. Palaeoclimatol. Palaeoecol.* **2019**, *516*, 166–178. [CrossRef]
27. Udaanjargal, U.; Hasebe, N.; Davaasuren, D.; Fukushi, K.; Tanaka, Y.; Gankhurel, B.; Katsuta, N.; Ochiai, S.; Miyata, Y.; Gerelmaa, T. Characteristics of Lake Sediment from Southwestern Mongolia and Comparison with Meteorological Data. *Geosciences* **2021**, *12*, 7. [CrossRef]
28. Shen, J. Spatiotemporal Variations of Chinese Lakes and Their Driving Mechanisms since the Last Glacial Maximum: A Review and Synthesis of Lacustrine Sediment Archives. *Chin. Sci. Bull.* **2013**, *58*, 17–31. [CrossRef]
29. Xiao, J.; Chang, Z.; Fan, J.; Zhou, L.; Zhai, D.; Wen, R.; Qin, X. The Link between Grain-size Components and Depositional Processes in a Modern Clastic Lake. *Sedimentology* **2012**, *59*, 1050–1062. [CrossRef]
30. Liu, J.; Wang, R.; Zhao, Y.; Yang, Y. A 40,000-Year Record of Aridity and Dust Activity at Lop Nur, Tarim Basin, Northwestern China. *Quat. Sci. Rev.* **2019**, *211*, 208–221. [CrossRef]
31. Wu, J.; Zeng, H.; Ma, L.; Bai, R. Recent Changes of Selected Lake Water Resources in Arid Xinjiang, Northwest China. *Quat. Sci.* **2012**, *32*, 142–150. Available online: https://kns.cnki.net/kcms2/article/abstract?v=m07J8nP_wCE7Lxd5TwpwK0Iu0KXJaoGyzBmXal_mr7cfG4eVBNv2yjZsrcDbOc8BThMZUJ_dLdSEgVn292rKr_9aiBYjJ5FblWqiWMo6qeU97EUostXElLJV2uXCtUjS3R3udJMZFIzNo_n8IPMYEfLRroxtbAzo56s9TK92v1I=&uniplatform=NZKPT&language=CHS (accessed on 1 April 2026).
32. Lan, J.; Xu, H.; Yu, K.; Sheng, E.; Zhou, K.; Wang, T.; Ye, Y.; Yan, D.; Wu, H.; Cheng, P.; et al. Late Holocene Hydroclimatic Variations and Possible Forcing Mechanisms over the Eastern Central Asia. *Sci. China Earth Sci.* **2019**, *62*, 1288–1301. [CrossRef]
33. Wang, Y.; Li, J.; Bao, A.; Hu, R.; Guo, M.; Zhao, S. Time-Series Analysis of Sayram Lake Area Changes during 1989–2014. *Arid. Land Geogr.* **2016**, *39*, 851–860. [CrossRef]
34. Jiang, Q.; Zheng, J.; Yang, Y.; Zhao, W.; Ning, D. A Persistently Increasing Precipitation Trend Through the Holocene in Northwest China Recorded by Black Carbon δ13C From Sayram Lake. *Front. Earth Sci.* **2020**, *8*, 228. [CrossRef]
35. Ma, L.; Wu, J.; Abuduwaili, J.; Liu, W. Aeolian Particle Transport Inferred Using a ~150-Year Sediment Record from Sayram Lake, Arid Northwest China. *J. Limnol.* **2015**, *74*, 1208. [CrossRef]
36. Chui, Y.; Zhou, W.; Cheng, P.; Yang, L.; Liu, X.; Lan, J.; Zhao, G.; Wu, S.; Fu, Y.; Xiong, X.; et al. Radiocarbon Chronology of Sediments with Implications for Climatic Events in Lop Nur, NW China. *J. Asian Earth Sci.* **2024**, *263*, 106024. [CrossRef]
37. Qiang, M.; Lang, W.; He, Z.; Jin, M.; Zhou, A.; Zhang, J. A 1600-Year Record of Eolian Activity from Jili Lake in Northern Xinjiang. *Quat. Int.* **2022**, *631*, 93–104. [CrossRef]
38. Zhang, J.; Xu, H.; Lan, J.; Ai, L.; Sheng, E.; Yan, D.; Zhou, K.; Yu, K.; Song, Y.; Zhang, S.; et al. Weakening Dust Storm Intensity in Arid Central Asia Due to Global Warming over the Past 160 Years. *Front. Earth Sci.* **2020**, *8*, 284. [CrossRef]
39. Zhou, G.; Huang, X.; Wang, Z.; Zhang, J.; Xie, H. Eolian Activity History Reconstructed by Bosten Lake Grain Size Data over the Past ~2000 Years. *J. Desert Res.* **2019**, *39*, 86–95. Available online: http://www.desert.ac.cn/EN/10.7522/j.issn.1000-694X.2018.00058 (accessed on 1 April 2026).
40. Dun, Y.; Luo, W.; Shao, M.; Wang, F.; Lu, J.; Li, D.; Man, D.; Che, X. Sand-Dust Horizontal Flux and Grain Size of Inland Lake Basin in Arid Region:A Case of Qingtu Lake. *J. Desert Res.* **2023**, *43*, 166–175. Available online: http://www.desert.ac.cn/EN/10.7522/j.issn.1000-694X.2023.00118 (accessed on 1 April 2026).
41. Wu, N.; Ge, Y.; Abuduwaili, J. Grain Size Characteristics of Sediments Found in Typical Landscapes in the Playa of Ebinur Lake, Arid Central Asia. *Land* **2021**, *10*, 1132. [CrossRef]
42. Song, Y. New Insights into Holocene Dust Activity in Eastern Uzbekistan. *Glob. Planet. Change* **2024**, *243*, 104633. [CrossRef]
43. Li, W.; Mu, G.; Ye, C.; Xu, L.; Li, G. Aeolian Activity in the Southern Gurbantunggut Desert of China during the Last 900 Years. *J. Arid. Land* **2023**, *15*, 649–666. [CrossRef]
44. Lin, Y.; Mu, G.; Chen, L.; Wu, C.; Xu, L. Sorting Characteristics and Its Implication of the Grain Size of Modern Atmospheric Dust Deposition near the Surface of the Cele Oasis, Xinjiang, China. *J. Desert Res.* **2022**, *42*, 139–146. Available online: http://www.desert.ac.cn/EN/10.7522/j.issn.1000-694X.2021.00140 (accessed on 1 April 2026).
45. Dong, Z.; Li, Z.; Xiao, C.; Wang, F.; Zhang, M. Characteristics of Aerosol Dust in Fresh Snow in the Asian Dust and Non-Dust Periods at Urumqi Glacier No. 1 of Eastern Tian Shan, China. *Environ. Earth Sci.* **2010**, *60*, 1361–1368. [CrossRef]
46. Liu, F.; Li, Z.; Hao, J.; Zhou, X.; Wang, F.; Zhang, H.; Wang, P.; Zhang, X.; Song, M.; Chen, T. Records of Inorganic Ions and Dust Particles in Snow at Yushugou Glacier No. 6 in the Desert Belt of Northwestern China. *Front. Earth Sci.* **2020**, *8*, 527493. [CrossRef]
47. Van Hengstum, P.J.; Reinhardt, E.G.; Boyce, J.I.; Clark, C. Changing Sedimentation Patterns Due to Historical Land-Use Change in Frenchman's Bay, Pickering, Canada: Evidence from High-Resolution Textural Analysis. *J. Paleolimnol.* **2007**, *37*, 603–618. [CrossRef]
48. Kumar, M.; Dashora, M.; Kumar, R.; Dubey, S.; Gupta, P.; Kumar, A. Deciphering Depositional Environment of Playa Lakes Using Grain Size Parameters in the Arid and Semi-Arid Region of Rajasthan, India. *Agriculture* **2022**, *12*, 2043. [CrossRef]
49. Weltje, G.J. End-Member Modeling of Compositional Data: Numerical-Statistical Algorithms for Solving the Explicit Mixing Problem. *Math. Geol.* **1997**, *29*, 503–549. [CrossRef]

50. Paterson, G.A.; Heslop, D. New Methods for Unmixing Sediment Grain Size Data. *Geochem. Geophys. Geosyst.* **2015**, *16*, 4494–4506. [CrossRef]
51. Leszczyńska, K.; Moskalewicz, D.; Stattegger, K. Statistical Approach to Identify Storm Deposits and Cryptic Event Layers from Grain-Size Data, Mechelinki, Poland, Baltic Sea. *Catena* **2024**, *242*, 108130. [CrossRef]
52. Xu, Y.; Zhao, H.; Liu, B.; Sun, A.; Wang, K.; Li, D.; Wei, J.; Ge, J. Development of a Physicochemical Proxy Index System for Surface Sediments in the Gurbantunggut Desert and Its Application to Regional Oasis-Desert Evolution. *Palaeogeogr. Palaeoclimatol. Palaeoecol.* **2025**, *662*, 112751. [CrossRef]
53. Zhang, X.; Yan, P.; Liu, X.; Dong, M.; Yuan, W.; Wang, X.; Zhang, C. Sediment Characteristics and Provenance of Riverine Dunes on the Lower Tora River in Qaidam Basin, China. *Geomorphology* **2025**, *478*, 109709. [CrossRef]
54. Niu, D.; Li, T.; Zhong, Y.; Liu, L.; Li, B. Study on Holocene Environmental Evolution Based on Grain Size End-Member Model: A Case Study of Two Outcrop Sections in Salawusu River Basin. *PLoS ONE* **2024**, *19*, e0305282. [CrossRef]
55. Liu, Y.; Liu, X.; Sun, Y. QGrain: An Open-Source and Easy-to-Use Software for the Comprehensive Analysis of Grain Size Distributions. *Sediment. Geol.* **2021**, *423*, 105980. [CrossRef]
56. Patrick, N.M.; Vats, N.; Bhaumik, A.K.; Mohanty, S.; Chattopadhyay, K. Plio-Pleistocene Sediment Grain Size Variability in the Western Bay of Bengal: Evidences of Indian Summer Monsoon Intensification. *Mar. Geol.* **2026**, *491*, 107682. [CrossRef]
57. Jiang, Q.; Ji, J.; Shen, J.; Matsumoto, R.; Tong, G.; Qian, P.; Ren, X.; Yan, D. Holocene Vegetational and Climatic Variation in Westerly-Dominated Areas of Central Asia Inferred from the Sayram Lake in Northern Xinjiang, China. *Sci. China Earth Sci.* **2013**, *56*, 339–353. [CrossRef]
58. Liu, X.; Herzschuh, U.; Shen, J.; Jiang, Q.; Xiao, X. Holocene Environmental and Climatic Changes Inferred from Wulungu Lake in Northern Xinjiang, China. *Quat. Res.* **2008**, *70*, 412–425. [CrossRef]
59. An, C.-B.; Zhao, J.; Tao, S.; Lv, Y.; Dong, W.; Li, H.; Jin, M.; Wang, Z. Dust Variation Recorded by Lacustrine Sediments from Arid Central Asia since ~15 Cal Ka BP and Its Implication for Atmospheric Circulation. *Quat. Res.* **2011**, *75*, 566–573. [CrossRef]
60. Blaauw, M.; Christen, J.A. Flexible Paleoclimate Age-Depth Models Using an Autoregressive Gamma Process. *Bayesian Anal.* **2011**, *6*, 457–474. [CrossRef]
61. Zhao, Q.; Zhen, X.; Zhou, L.; Wang, H.; Lv, H.; Chen, Y.; Ren, S. Grain Size End Member Characteristics and Paleoclimatic Significance of Loess Deposit in Shengshan Island during the Last Glacial Period. *Acta Sedimentol. Sin.* **2024**, *42*, 521–533. [CrossRef]
62. Yuan, R.; Feng, W.; Zhang, C.; Zhao, K.; Liu, J.; Fu, W.; Wang, Z.; Meng, Q.; Wang, L. Fluvial—Aeolian Dune Depositional Environment Significances from Grain-Size End-Member in Low-Beach at the Head of Tianxing Central-Bar in Wuhan Section of Yangtze River. *Geol. Rev.* **2024**, *70*, 436–448. [CrossRef]
63. Udden, J.A. Mechanical Composition of Clastic Sediments. *Geol. Soc. Am. Bull.* **1914**, *25*, 655–744. [CrossRef]
64. Wentworth, C.K. A Scale of Grade and Class Terms for Clastic Sediments. *J. Geol.* **1922**, *30*, 377–392. [CrossRef]
65. Folk, R.L.; Ward, W.C. Brazos River Bar: A Study in the Significance of Grain Size Parameters. *J. Sediment. Res.* **1957**, *27*, 3–26. [CrossRef]
66. Wei, X.; Jiang, H.; Shi, W.; Fan, J.; Xu, H.; Hu, W.; Chang, X.; Huang, S.; Guo, Q.; Zhang, S.; et al. Earthquake Supercycles and Fault Interaction over the Past 32 Ka in the Lake Ebinur Area, Xinjiang, China. *Sci. Total Environ.* **2024**, *927*, 172052. [CrossRef] [PubMed]
67. Dietze, E.; Maussion, F.; Ahlborn, M.; Diekmann, B.; Hartmann, K.; Henkel, K.; Kasper, T.; Lockot, G.; Opitz, S.; Haberzettl, T. Sediment Transport Processes across the Tibetan Plateau Inferred from Robust Grain-Size End Members in Lake Sediments. *Clim. Past* **2014**, *10*, 91–106. [CrossRef]
68. Vandenberghe, J. Grain Size of Fine-Grained Windblown Sediment: A Powerful Proxy for Process Identification. *Earth-Sci. Rev.* **2013**, *121*, 18–30. [CrossRef]
69. Pye, K.; Tsoar, H. The Mechanics and Geological Implications of Dust Transport and Deposition in Deserts with Particular Reference to Loess Formation and Dune Sand Diagenesis in the Northern Negev, Israel. *Geol. Soc. London Spéc. Publ.* **1987**, *35*, 139–156. [CrossRef]
70. Qiang, M.; Chen, F.; Zhang, J.; Zu, R.; Jin, M.; Zhou, A.; Xiao, S. Grain Size in Sediments from Lake Sugan: A Possible Linkage to Dust Storm Events at the Northern Margin of the Qinghai–Tibetan Plateau. *Environ. Geol.* **2007**, *51*, 1229–1238. [CrossRef]
71. Vyse, S.A.; Herzschuh, U.; Andreev, A.A.; Pestryakova, L.A.; Diekmann, B.; Armitage, S.J.; Biskaborn, B.K. Geochemical and Sedimentological Responses of Arctic Glacial Lake Ilirney, Chukotka (Far East Russia) to Palaeoenvironmental Change since ~51.8 Ka BP. *Quat. Sci. Rev.* **2020**, *247*, 106607. [CrossRef]
72. Chen, Y.; Liu, X. Aeolian Activity in Arid Central Asia during the Past 4,0000 Years Inferred from Lake Ailike, Xinjiang. *Catena* **2023**, *227*, 107106. [CrossRef]
73. Zhou, J.; Wu, J.; Ma, L.; Qiang, M. Late Quaternary Lake-Level and Climate Changes in Arid Central Asia Inferred from Sediments of Ebinur Lake, Xinjiang, Northwestern China. *Quat. Res.* **2019**, *92*, 416–429. [CrossRef]

74. Dietze, E.; Hartmann, K.; Diekmann, B.; IJmker, J.; Lehmkuhl, F.; Opitz, S.; Stauch, G.; Wünnemann, B.; Borchers, A. An End-Member Algorithm for Deciphering Modern Detrital Processes from Lake Sediments of Lake Donggi Cona, NE Tibetan Plateau, China. *Sediment. Geol.* **2012**, *243–244*, 169–180. [CrossRef]
75. Zhang, Y.; Mao, C.; Zhang, J.; Huang, X. Otgonbayar Demberel Aeolian Activities in the NW Mongolia during the Holocene Recorded by Grain-Sizesensitive Particles in the Sediments of Lake Tolbo. *J. Lake Sci.* **2023**, *35*, 368–380. Available online: https://www.sciengine.com/JLSci/doi/10.18307/2023.0129 (accessed on 1 April 2026).
76. Qiang, M.; Liu, Y.; Jin, Y.; Song, L.; Huang, X.; Chen, F. Holocene Record of Eolian Activity from Genggahai Lake, Northeastern Qinghai-Tibetan Plateau, China. *Geophys. Res. Lett.* **2014**, *41*, 589–595. [CrossRef]
77. Gao, F.; Zheng, X.; Jia, J.; Li, K.; Xia, D.; Yang, J.; Lu, H.; Shi, F.; Chen, Z.; Wang, S. Evolution of Near-Surface Wind Strength in Northeastern Arid Central Asia During the Holocene. *Paleoceanography* **2021**, *36*, e2020PA003970. [CrossRef]
78. Zhang, J.; Huang, X.; Qiang, M.; Demberel, O.; Wang, W.; Zheng, M.; Xiang, L.; Hu, Y.; Xiao, J. Increasing Spring Insolation in the Late Holocene Intensified Aeolian Activity in Dryland Asia. *Geophys. Res. Lett.* **2022**, *49*, e2022GL101777. [CrossRef]
79. Saimaiti, A.; Fu, C.; Song, Y.; Shukurov, N. Spatial Distribution, Material Composition and Provenance of Loess in Xinjiang, China: Progress and Challenges. *Atmosphere* **2022**, *13*, 1790. [CrossRef]
80. Lehmkuhl, F.; Haselein, F. Quaternary Paleoenvironmental Change on the Tibetan Plateau and Adjacent Areas (Western China and Western Mongolia). *Quat. Int.* **2000**, *65–66*, 121–145. [CrossRef]
81. Yamaguchi, N.; Ando, T.; Enokida, H.; Nakada, N.; Yamaki, S.; Ohta, T. Logratio Analysis of Components Separated from Grain-size Distributions and Implications for Sedimentary Processes: An Example of Bottom Surface Sediments in a Shallow Lake. *Sedimentology* **2024**, *71*, 1291–1304. [CrossRef]
82. Xi, C.; Zuo, H.; Yan, M.; Yan, Y. Grain Size Characteristics of Different Types of Surface Sediments around Qixing Lake in Kubuqi Desert. *Front. Environ. Sci.* **2024**, *12*, 1409260. [CrossRef]
83. Nord, M.A.; Maier, M.A.; Bijak, A.L.; Crane, J.L.; Pollard, A.I. Assessment of Recent Lake Sediment Conditions in the Conterminous U.S. *Sci. Total Environ.* **2024**, *956*, 177315. [CrossRef]
84. Wang, X. Preliminary Study on the Environment Recovering Methods of Ebinur Lake. *J. Hebei Univ. Environ. Eng.* **2011**, *21*, 29–31+36. [CrossRef]
85. Yang, Q.; He, Q.; Li, H.; Lei, J. Study on the Sand-Dust Climate Change Trend and Jump in Ebinur Lake Area. *J. Desert Res.* **2003**, *23*, 27–32. [CrossRef]
86. Li, Z.; Tan, C.; Yang, J.; Zhao, T.; He, Q.; Meng, L.; Zhang, L.; Luo, Y.; Lu, Z.; Wang, D. Spatial and Temporal Variations of Dust Storms in Xinjiang in the 21st Century and the Key Meteorological Influence Factors. *Acta Sci. Circumstantiae* **2024**, *44*, 1–9. [CrossRef]
87. Sabatier, P.; Moernaut, J.; Bertrand, S.; Van Daele, M.; Kremer, K.; Chaumillon, E.; Arnaud, F. A Review of Event Deposits in Lake Sediments. *Quaternary* **2022**, *5*, 34. [CrossRef]
88. Leithold, E.; Wegmann, K.; Bohnenstiehl, D.; Slajus, L.; Contreras, T. A Late Holocene Sedimentary Record of Earthquakes and Hydroclimate from Ozette Lake, Washington, USA. *Quat. Res.* **2025**, *127*, 90–106. [CrossRef]
89. Schnellmann, M.; Anselmetti, F.S.; Giardini, D.; McKenzie, J.A.; Ward, S.N. Prehistoric Earthquake History Revealed by Lacustrine Slump Deposits. *Geology* **2002**, *30*, 1131. [CrossRef]
90. Lan, J.; Wang, T.; Dong, J.; Kang, S.; Cheng, P.; Zhou, K.; Liu, X.; Wang, Y.; Ma, L. The Influence of Ice Sheet and Solar Insolation on Holocene Moisture Evolution in Northern Central Asia. *Earth-Sci. Rev.* **2021**, *217*, 103645. [CrossRef]
91. Ran, M.; Feng, Z. Holocene Moisture Variations across China and Driving Mechanisms: A Synthesis of Climatic Records. *Quat. Int.* **2013**, *313–314*, 179–193. [CrossRef]
92. Lv, Y.; Zhao, J.; Huang, W.; Tao, S.; An, C. Decomposition of the Grain-Size Component and Its Climate Implication from Lake Barkol, Xinjiang. *Acta Sedimentol. Sin.* **2011**, *29*, 134–142. [CrossRef]
93. Yao, T.; Wu, G.; Pu, J.; Jiao, K.; Cuilan, C. Relationship between Calcium and Atmospheric Dust Recorded in Guliya Ice Core. *Chin. Sci. Bull.* **2004**, *49*, 706–710. [CrossRef]
94. Chen, S.; Huang, J.; Kang, L.; Wang, H.; Ma, X.; He, Y.; Yuan, T.; Yang, B.; Huang, Z.; Zhang, G. Emission, Transport, and Radiative Effects of Mineral Dust from the Taklimakan and Gobi Deserts: Comparison of Measurements and Model Results. *Atmos. Chem. Phys.* **2017**, *17*, 2401–2421. [CrossRef]
95. Cheng, L.; Song, Y.; Yang, L.; Chang, H.; Wu, Y.; Long, H.; Miao, X.; Dong, Z. Variations of the Intensity of the Siberian High During the Last Glacial Revealed by the Sorting Coefficient of Loess-Paleosol Deposits in Eastern Central Asia. *Paleoceanog. Paleoclimatol.* **2022**, *37*, e2022PA004468. [CrossRef]
96. Mayewski, P.A.; Meeker, L.D.; Twickler, M.S.; Whitlow, S.; Yang, Q.; Lyons, W.B.; Prentice, M. Major Features and Forcing of High-latitude Northern Hemisphere Atmospheric Circulation Using a 110,000-year-long Glaciochemical Series. *J. Geophys. Res.* **1997**, *102*, 26345–26366. [CrossRef]
97. Bond, G.; Kromer, B.; Beer, J.; Muscheler, R.; Evans, M.N.; Showers, W.; Hoffmann, S.; Lotti-Bond, R.; Hajdas, I.; Bonani, G. Persistent Solar Influence on North Atlantic Climate During the Holocene. *Science* **2001**, *294*, 2130–2136. [CrossRef]

98. Parrenin, F.; Bouchet, M.; Buizert, C.; Capron, E.; Corrick, E.; Drysdale, R.; Kawamura, K.; Landais, A.; Mulvaney, R.; Oyabu, I.; et al. The Paleochrono-1.1 Probabilistic Model to Derive a Common Age Model for Several Paleoclimatic Sites Using Absolute and Relative Dating Constraints. *Geosci. Model Dev.* **2024**, *17*, 8735–8750. [CrossRef]
99. Vandergoes, M.J.; Howarth, J.D.; Dunbar, G.B.; Turnbull, J.C.; Roop, H.A.; Levy, R.H.; Li, X.; Prior, C.; Norris, M.; Keller, L.D.; et al. Integrating Chronological Uncertainties for Annually Laminated Lake Sediments Using Layer Counting, Independent Chronologies and Bayesian Age Modelling (Lake Ohau, South Island, New Zealand). *Quat. Sci. Rev.* **2018**, *188*, 104–120. [CrossRef]
100. Huang, X.Z.; Chen, F.H.; Fan, Y.X.; Yang, M.L. Dry Late-Glacial and Early Holocene Climate in Arid Central Asia Indicated by Lithological and Palynological Evidence from Bosten Lake, China. *Quat. Int.* **2009**, *194*, 19–27. [CrossRef]
101. Berger, A.; Loutre, M.F. Insolation Values for the Climate of the Last 10 Million Years. *Quat. Sci. Rev.* **1991**, *10*, 297–317. [CrossRef]
102. De Boer, B.; Lourens, L.J.; Van De Wal, R.S.W. Persistent 400,000-Year Variability of Antarctic Ice Volume and the Carbon Cycle Is Revealed throughout the Plio-Pleistocene. *Nat. Commun.* **2014**, *5*, 2999. [CrossRef]
103. Li, Y.; Song, Y.; Yin, Q.; Han, L.; Wang, Y. Orbital and Millennial Northern Mid-Latitude Westerlies over the Last Glacial Period. *Clim. Dyn.* **2019**, *53*, 3315–3324. [CrossRef]
104. Hao, Q.; Wang, L.; Oldfield, F.; Peng, S.; Qin, L.; Song, Y.; Xu, B.; Qiao, Y.; Bloemendal, J.; Guo, Z. Delayed Build-up of Arctic Ice Sheets during 400,000-Year Minima in Insolation Variability. *Nature* **2012**, *490*, 393–396. [CrossRef]
105. Machalett, B.; Oches, E.A.; Frechen, M.; Zöller, L.; Hambach, U.; Mavlyanova, N.G.; Marković, S.B.; Endlicher, W. Aeolian Dust Dynamics in Central Asia during the Pleistocene: Driven by the Long-term Migration, Seasonality, and Permanency of the Asiatic Polar Front. *Geochem. Geophys. Geosyst.* **2008**, *9*, 2007GC001938. [CrossRef]
106. Perşoiu, A.; Ionita, M.; Weiss, H. Atmospheric Blocking Induced by the Strengthened Siberian High Led to Drying in West Asia during the 4.2 Ka BP Event—A Hypothesis. *Clim. Past* **2019**, *15*, 781–793. [CrossRef]
107. Wirth, S.B.; Glur, L.; Gilli, A.; Anselmetti, F.S. Holocene Flood Frequency across the Central Alps—Solar Forcing and Evidence for Variations in North Atlantic Atmospheric Circulation. *Quat. Sci. Rev.* **2013**, *80*, 112–128. [CrossRef]
108. Wang, Z.; Liu, X.; Xie, H.; Chen, S.; Chen, J.; Wang, H.; Ma, M.; Chen, F. Time-Transgressive Onset of Holocene Climate Optimum in Arid Central Asia and Its Association with Cultural Exchanges. *Land* **2024**, *13*, 356. [CrossRef]
109. Cai, Y.; Chiang, J.C.H.; Breitenbach, S.F.M.; Tan, L.; Cheng, H.; Edwards, R.L.; An, Z. Holocene Moisture Changes in Western China, Central Asia, Inferred from Stalagmites. *Quat. Sci. Rev.* **2017**, *158*, 15–28. [CrossRef]
110. Li, Y.; Song, Y.; Fitzsimmons, K.E.; Chang, H.; Orozbaev, R.; Li, X. Eolian Dust Dispersal Patterns since the Last Glacial Period in Eastern Central Asia: Insights from a Loess-Paleosol Sequence in the Ili Basin. *Clim. Past* **2018**, *14*, 271–286. [CrossRef]
111. Li, Y.; Song, Y.; Xiao, J.; Zong, X.; Li, Y. Precipitation Changes during the Last Glacial Period in the Ili Basin, Northern Central Asia, as Inferred from the Records of Loess Dolomite. *Glob. Planet. Change* **2024**, *242*, 104599. [CrossRef]
112. Zheng, C.; Zhang, Z.; Kong, X.; Granger, D.; Zhao, Z.; Zhang, Z. Spatiotemporal Glacier Retreat on the Tibetan Plateau since the LGMG to Early Holocene Based on Compilation of Moraine Boulder Ages. *Sci. Rep.* **2025**, *15*, 3723. [CrossRef]
113. Van Woerkom, T.; Steiner, J.F.; Kraaijenbrink, P.D.A.; Miles, E.S.; Immerzeel, W.W. Sediment Supply from Lateral Moraines to a Debris-Covered Glacier in the Himalaya. *Earth Surf. Dyn.* **2019**, *7*, 411–427. [CrossRef]
114. Orme, L.C.; Charman, D.J.; Reinhardt, L.; Jones, R.T.; Mitchell, F.J.G.; Stefanini, B.S.; Barkwith, A.; Ellis, M.A.; Grosvenor, M. Past Changes in the North Atlantic Storm Track Driven by Insolation and Sea-Ice Forcing. *Geology* **2017**, *45*, 335–338. [CrossRef]
115. Kang, S.; Du, J.; Wang, N.; Dong, J.; Wang, D.; Wang, X.; Qiang, X.; Song, Y. Early Holocene Weakening and Mid- to Late Holocene Strengthening of the East Asian Winter Monsoon. *Geology* **2020**, *48*, 1043–1047. [CrossRef]
116. Chen, S.; Chen, J.; Lv, F.; Liu, X.; Huang, W.; Wang, T.; Liu, J.; Hou, J.; Chen, F. Holocene Moisture Variations in Arid Central Asia: Reassessment and Reconciliation. *Quat. Sci. Rev.* **2022**, *297*, 107821. [CrossRef]
117. Qiang, M.; Jin, Y.; Liu, X.; Song, L.; Li, H.; Li, F.; Chen, F. Late Pleistocene and Holocene Aeolian Sedimentation in Gonghe Basin, Northeastern Qinghai-Tibetan Plateau: Variability, Processes, and Climatic Implications. *Quat. Sci. Rev.* **2016**, *132*, 57–73. [CrossRef]